STATE ESTIMATION OF AN ACOUSTIC BUBBLE-POWERED

MICROSWIMMER FROM ULTRASOUND IMAGING DATA

by

Zunding Xiao

BS in Automobile Engineering, Chongqing University of Technology, 2009

MS in Mechanical Engineering, Swansea University, 2013

Submitted to the Graduate Faculty of

the Swanson School of Engineering in partial fulfillment

of the requirements for the degree of

Master of Science in Mechanical Engineering

University of Pittsburgh

2018

UNIVERSITY OF PITTSBURGH

SWANSON SCHOOL OF ENGINEERING

This thesis was presented

by

Zunding Xiao

It was defended on

July 24, 2018

and approved by

Nitin Sharma, PhD, Assistant Professor

Sung Kwon Cho, PhD, Associate Professor

Kang Kim, PhD, Associate Professor

Thesis Advisor: Nitin Sharma, PhD, Assistant Professor

STATE ESTIMATION OF AN ACOUSTIC BUBBLE-POWERED MICROSWIMMER

FROM ULTRASOUND IMAGING DATA

Zunding Xiao, M.S

University of Pittsburgh, 2018

Tiny and untethered robots can navigate into narrow blood arteries and in vivo tissues. Such a revolutionary device brings the possibility of delivering drugs to a specific target and medical diagnosis of diseases that may not be feasible with conventional treatment and diagnosis. Current medical micro-robot technology uses externally-generated magnetic fields. The actuation technology, although external to the micro-robot, is expensive and bulky. There is also always a risk of damaging human tissues with this technique. A promising recent technology uses acoustic waves as a power source for a micro swimming robot. An acoustic power source is extremely small compared to a magnetic field power source and there is a very little risk of any damage to the tissues during the micro-robot actuation. This thesis presents dynamic modeling and state estimation of a novel underwater swimming micro-robot that is powered through oscillations of gas bubbles trapped inside the micro-robot.

The rectangular shaped, which is made of photoresist, has the dimensions of 950 μm × 460 μm × 340 μm. The motion is produced by the oscillations of gaseous bubbles trapped in the micro-tubes. Primarily acoustic waves induce oscillations at a certain frequency and thus are used as a propulsion mechanism to realize 3 degree-of-freedom swimming motion. Ultrasound imaging is proposed to sense the swimming motion of the micro-robot.

The main focus of the thesis is on the development of an estimator that detects swimming motion of the micro-robot from ultrasound imaging data. A new class of nonlinear state estimation method, called state-dependent coefficient (SDC) estimator, is implemented to improve the accuracy of micro-robot state estimation. The estimator is also used to predict rotation of the robot, which cannot be measured by ultrasound imaging due to the robot's extremely small size. Experiments and simulations were carried out to verify the accuracy of the estimator and the performance of the estimator coupled with a closed-loop controller.

A dynamic model that captures the acoustic actuation was also developed. The model is used in the SDC estimator and was also used to develop a nonlinear control law that tracks a desired swimming motion. The model includes a switching mechanism that was designed to produce bidirectional swimming motion (e.g., left turn and right turn). Each channel that holds the gas bubbles can produce only unidirectional movement. The mechanism switches between counteracting tubes to produce bidirectional movement. The input switch mechanism was demonstrated in a simulation study of the micro-swimmer.

TABLE OF CONTENTS

LIST OF TABLES

LIST OF FIGURES

1.0   INTRODUCTION

Miniature medical robotics extend our interaction with micro/nano scale entities inside the human body. It allows access, manipulation, and exploration at a scale that macroscale robots are not capable of. Whether diagnosing poor oxygen supply in eyes or sensing diseases in the GI tract, microscale untethered robots are becoming more mobile, better communicators, and more precise. The concept of microscale robots was popularized by the 1960s classic movie "Fantastic Voyage". After decades of research, numerous types of microscale robots have been developed and applied. However, their manipulation is still challenging.

The main motivation for modeling and controlling the microscale robot is to develop a feasible manipulation scheme for medical procedures such as drug delivery, microsurgery, bio-sensing, imaging, etc. The robot aims to access small (less than 1 mm in all dimension) [1] spaces, operate untethered, and swim through narrow aisles in microfluidics. To perform less than a millimeter size medical operations, *in vivo*, accurate control, command, and estimation methods for both translational and rotational motions are required. Thus bringing about critical challenges in a micro-robot development that include design of a dynamic structure with a corresponding actuation mechanism, as well as strategies for detection and communication with the robot inside the human body.

1.1 MOTIVATIONS FOR ACOUSTIC ACTUATION AND ULTRASOUND IMAGING-BASED FEEDBACK

Acoustic actuation has recently been proven as an efficient way to drive micro-robots. In [2], an acoustic scallop was built. The device contained a periodically oscillating gaseous bubble that was externally excited by acoustic waves in a certain Reynolds number environment. Such a condition results in a flow asymmetry due to an unsustainable pressure gradient when a fluid leaves the tube end. Thus when the bubble trapped in the tube compresses and expands in an ambient sound field, intake and discharge of the nearby liquid flow pushes the device to move. Experiments showed the reliability and controllability of this [3], [4]. Using the same principles, a focused ultrasonic wave can also be used to excite the bubbles.

1.1.1 Ultrasound actuation

Ultrasound, which refers to acoustic waves with frequency higher than 20kHz, is ubiquitously exploited in medical and clinical applications. Unlike bulky magnetic field actuators, power transmitted from medical ultrasound machine is, in general, safe, non-ionizing and efficient to utilize. The main motivation of ultrasound is that it can be implemented as an actuation source and simultaneously used as an imaging feedback to control a micro-robot operating *in vivo*.

1.1.2 Imaging tracking

As an imaging modality, ultrasound is a mature technique that provides real-time vision information with high resolution and good signal to noise ratio (SNR). Using proper tracking

algorithms, such as optical flow and active contour based methods [5]–[9], ultrasound image is reliable for fast motion estimation. These methods, mainly, developed in computer vision, detect frame to frame object positions based on conservation of brightness and then estimate instantaneous velocity field.

1.2   MOTIVATIONS FOR STATE ESTIMATION

Although ultrasound technique is capable of capturing high resolution image, but the accuracy of small object motion tracking from conventional B-mode ultrasound image is limited by speckle noise, inevitable brightness variation, and other image artifacts. Moreover, ultrasound image tracking can hardly provide rotational feedback of compact object. Therefore, the main motivation of state estimation is to obtain accurate object motion information and to obtain estimation of unmeasurable state variables.

1.3   THESIS CONTRIBUTIONS

The contribution of this thesis is that a state dependent coefficient (SDC) estimator is applied to estimate the states of a micro-swimmer from ultrasound imaging data during experiment. An open-loop experiment was performed and both camera and ultrasound imaging were used, during the experiment, to capture the micro-swimmer motion and to generate ultrasound images. Position and velocity measurements were acquired by an image tracking algorithm through the recorded ultrasound imaging data. These measured state variables from camera were used later

as the bench mark and these from ultrasound imaging were used as measurements to the SDC estimator. The dynamic model of the micro-swimmer is built upon work in [3]. 5 SDC parameterized matrices were derived from the swimmer dynamics for the estimation. The performance of estimation was evaluated by comparing the result to the bench mark and measurement. The result strengthens the benefit of using SDC estimator. The dynamic model of SDC does not require Jacobian linearization and the nonlinear model can be parameterized into state dependent matrices using extended linearization. Hence, it can provide improved performance compared to the Kalman filter [10], [11], which is applicable to only linear systems and an extended Kalman filter (EKF), which uses a linearized model of a nonlinear dynamics to estimate state. Therefore SDC estimated state was also compared with the state estimated from EKF.

Further, a developed nonlinear controller and estimator coupled model was derived. A closed-loop simulation was built to test the performance of the control system. The control objective was to achieve a tracking task with the estimated state derived from ultrasound imaging as the sole feedback signal. Simulation result validates that the proposed approach is feasible to run the swimmer over a designed trajectory. In addition, a designed input switch mechanism was also proved to be capable of producing bidirectional swimming motion from counteracting tubes that produce motion in only one direction.

2.0   BACKGROUND INFORMATION AND LITERATURE REVIEW

This chapter introduces the background knowledge that was used to develop the modeling and control strategy proposed in this thesis. A number of related works were mentioned and compared in the following section. Since all of these works showed specific disadvantage, new propulsion method and corresponding control scheme were proposed.

2.1   STATE OF THE ART

Medical applications that need to be carried out in inaccessible organs or tissue parts have led to development of micro-robots in recent years [1], [12], [13]. Various micro-robot propulsion and actuation mechanisms have been developed. Guo proposed a new prototype of driven by bionics propulsion forces in [14]. The fish-like underwater swimmer used an ionic conducting polymer film (ICPF) actuator as the servo actuator. There were two tails with a fin driven respectively on the swimmer to realize motion in three degrees of freedom. Nevertheless, such indirect motion mechanism would either decrease the mobility of the swimmer or increase the complexity of control strategy. More, due to the need of extremely small size, placing actuation mechanisms inside the micro-swimmer is not feasible. Guo's design with ICPF actuator mounted on the swimmer body would be hard or not cost-efficient to be manufactured into smaller size.

In [15], a helical propellers that mimic bacterial flagella was developed by Dreyfus. The helically shaped swimmer had a linear chain of colloidal magnetic particles which were linked by DNA and attached to a red blood cell. An external uniform magnetic field was used to control the chain to act as a flexible artificial flagellum. The swimmer successfully realized motions in two dimensional space and three degrees of freedom. However, besides the potential mobility issue that the swimmer cannot take rapid turn, the superparamagnetic colloids made filaments were produced through the specific biotin–streptavidin interaction, the expediency of aforementioned procedure and the strength of the binding between magnetic particles were concerning issues.

External magnetic field is actually an ideal method to drive wirelessly. It avoids the need to place on-board actuators and energy sources [1], [16], [17]. Micro-swimmers in these studies had flagellum-like propellers and were driven by an electromagnetic coil set. The external magnetic actuation provided a direct way of controlling and steering their micro-swimmers. External magnetic field was also exerted on micro-swimmers that were tailless. In [18], [19], swimmers were designed to be a rigid object and directly pulled by magnetic field gradients. Their works presented a more straightforward swimmer dynamic relation to the magnetic field than that of swimmers equipped with tails or flagellums since these tailless swimmers are directly pushed by the magnetic force. Nevertheless, high magnetic field gradients were required to manipulate the swimmer at a distance. Generating such a fast changing magnetic field might cause damage to human tissues by heat.

An electrostatic field approach has also been used as a propulsion mechanism. In [20], Donald presented an electrostatic micro-swimmer. It consisted of an untethered scratch drive actuator and a cantilevered steering arm. Both components were powered through a capacitive

coupling with an interdigitated electrode array. Although it eliminated the risk of implementing a magnetic field, it was restricted by a few control issues including the issue that only unidirectional movement could be achieved.

It appears that, existing micro-swimmers have a variety of different swimming styles and their corresponding propulsion methods. A comparison of different swimming methods was made in [21]. It was concluded that helical-propeller and elastic-tail swimmers outperformed those swimmers that are pulled by a field gradient. Further, the author believed that swimming using helical propellers were the most promising devices due to multiple potential benefits. Despite this, these propulsion mechanisms still have unfavorable implementation aspects. These issues can be concluded as follows:

1. Magnetic and electrostatic field gradients can damage tissues due to heating and ionization.

2. Propellers have problems such as low propulsion efficiency, difficulties in positioning, agile turning, and precise hovering.

3. Expensive and bulky apparatus might be required to operate a micro-swimmer in a distance.

In addition, neither of these works have studied methods for detecting and communicating with micro-swimmers inside dark areas. Since electron microscope is unavailable without illumination, feasible method of detecting a microscale robot is needed.

2.2   ACOUSTIC PROPULSION AND IMAGING METHOD

2.2.1   The 'acoustic scallop'

In 2006, Dijkink [2] carried out a preliminary experiments of a novel bubble-powered device. The author was inspired by a common fluid mechanical fact that fluid pushed out of a tube forms a jet in certain Reynolds number condition.

2.2.2   Acoustic Bubble-powered Swimmer

Experiments showed the reliability and controllability of this micro-swimmer [3], [4]. Using the same principles, a focused ultrasonic wave can also be used to excite the bubbles. Ultrasound, which refers to acoustic waves with frequency higher than 20 kHz, is ubiquitously exploited in medical and clinical applications. Unlike bulky magnetic field actuators, power transmitted from medical ultrasound machine is, in general, safe, non-ionizing and efficient to utilize. The advantage of ultrasound is that it can be implemented simultaneously used as a micro-robots' power source and as imaging feedback to control the micro-robot.

2.3   ULTRASOUND IMAGE AND MOTION TRACKING ALGORITHM

Ultrasound image is an ideal tool to detect an object inside a living organism. Ultrasound imaging provides real-time vision information with high resolution and good signal to noise ratio (SNR). Theoretically, by using proper tracking algorithms, the object's state of interest can be

detected and estimated. However, existing techniques are largely based on algorithms developed for a digital video camera [22]. Strong assumptions such as smoothness of motion, minimal amount of occlusion, illumination constancy, high contrast with respect to background, etc. are made for these tracking algorithms. Nonetheless, ultrasound image differs from video image in many ways. According to [9], the difference between ultrasound image and visual scene image can be summarized in Table 1.

Table 1. Comparison of Scene-Oriented and Ultrasonic Image Sequences

	Visual Scene Image Sequence	Ultrasound Image Sequence
Image capture	Camera	Ultrasound scanner
Image plane	Perspective projection of 3-D objects	Cross section of 3-D tissue structures
Intensity function	Smooth, slow varying across objects	Speckle-like pattern, rapidly varying
Motion types	Translation + rotation rigid	Translation + rotation + deformation
Typical resolution	Pixel resolution (approx.)	Pulse dimension resolution
Challenges	Changes in external illumination, occlusion, aperture problems, no gray value changes	Low SNR, speckle decorrelation, motion ambiguities, spatial aliasing

It can be concluded that ultrasound image sequence is quite different from visual scene image sequence. Hence, the current tracking algorithms would bring problems when applied on ultrasound image to track movement of speckle. And challenges of tracking speckles can be summarized as

- Target deformation

- Noisy images

- Motion ambiguities

- Spatial aliasing

- Speckle decorrelation

- Out-of-plane motion

- Speckle motion artifacts

- Quantization error

To deal the above problems, five feature tracking methods were presented and compared in [23]. They were (1) the modified cross-correlation algorithm, (2) the sequential similarity detection (SSD) algorithm, (3) the Star algorithm, (4) the Star-Kalman algorithm and (5) the discrete snake algorithm.

The cross correlation approach is the normalized cross-correlation technique from [24]. The method evaluates point displacement by shifting current image sub-block in its neighborhood and searching for a best correlated match based on prior image frame. This method has a good resistance for drift but it is very sensitive to image deformation.

The sequential similarity detection (SSD) method from [25] can be used to track arbitrary features in ultrasound images. The method uses motion-energy detection principle. Similar to cross correlation approach, a current sub-block of the image is shifted in its neighborhood, but the difference is to search for a minimum absolute subtraction (pixel by pixel) based on a prior fixed sub-block frame.

In [26], the author implemented a Star algorithm to observe the carotid artery in real-time. This method applies an edge-detection filter to detect the target boundary along rays emanating from a point interior to the carotid artery. It determines center coordinates of the cavity as the center of gravity of extracted boundary points. Although the Star algorithm can perform in real-time and is robust to cumulative error, it is relatively unstable. This is because the algorithm does not incorporate estimates that are calculated from previous frames.

An improved method, which is called Star-Kalman, was developed by combining the Star algorithm and a Kalman filter. It applies the edge function from the previous method to all the pixels along each individual target radius then chooses those points with highest edge function value to be the estimated contour.

The Discrete Snake Model is a modified algorithm originated from [7]. The method implements similar principle from the Star algorithm to find edge points instead of performing snake deformation on the original image. However, the algorithm easily loses the feature and diverges when target moves at high speed (100 pixels/s). Compared to the SSD and the Star-Kalman algorithms which can be used with a small error to track features in ultrasound images at different velocities, the Snake algorithm is the least reliable one

2.4   STATE ESTIMATION

Previous section implied that the accuracy of small object motion tracking from conventional B-mode ultrasound image is limited by plenty of factors. Therefore, to obtain accurate and full object motion and state information, a state estimator is required to assist in image tracking algorithm.

2.4.1   State-Dependent Coefficient Estimator

In 1962, Pearson [27] proposed a time- and state-dependent formulation of nonlinear and non-autonomous system and suggested treating it as an instantaneous linear time invariant system. Thus, the resultant problem could be solved by an LQR technique. The framework has now

developed into a celebrated state-dependent Riccati equation approach, and it has gained immense popularity in various domains [28].

In [11], [10], a state-dependent coefficient (SDC) estimator to accurately predict joint angles from inertial measurement unit (IMU) sensor measurement was proposed and implemented. The estimator successfully eliminated the measurement noise, drift, and external interference of the IMU and thus significantly improved the performance of the control system. The authors indicated that SDC estimator is robust to uncertainties in the motion modeling and noise from the measurements. Experiment results in [10] validated that SDC estimator has outperformed the EKF in accuracy.

A vehicle state estimation was also developed using the same technique [29]. In this work, a state estimator of a collision avoidance controller was implemented to estimate those vehicle states that were not measurable. Both the SDC estimator and the EKF were utilized to work in under same condition. Experiment results showed similar performance in terms of the resulting estimates. However, it was noticeable that the SDC estimator only required 21% of the computation time needed by the EKF.

3.0   MICRO-SWIMMER DESIGN

In this section dynamic model of the micro-swimmer is described, device specification and mathematical model are described in detail. Figure 1 shows the three dimensional (3D) view of the micro-swimmer. It consists of the swimmer body, one tube at the back, and two tube sets on lateral sides. Those micro-tubes are closed at one end and partially filled with gas. External sound waves actuate the gas volume that expels and draws liquid through the open end of the tube, which drives the micro-swimmer to move. The six sets of pins were designed to reduce the effect of resistance force.
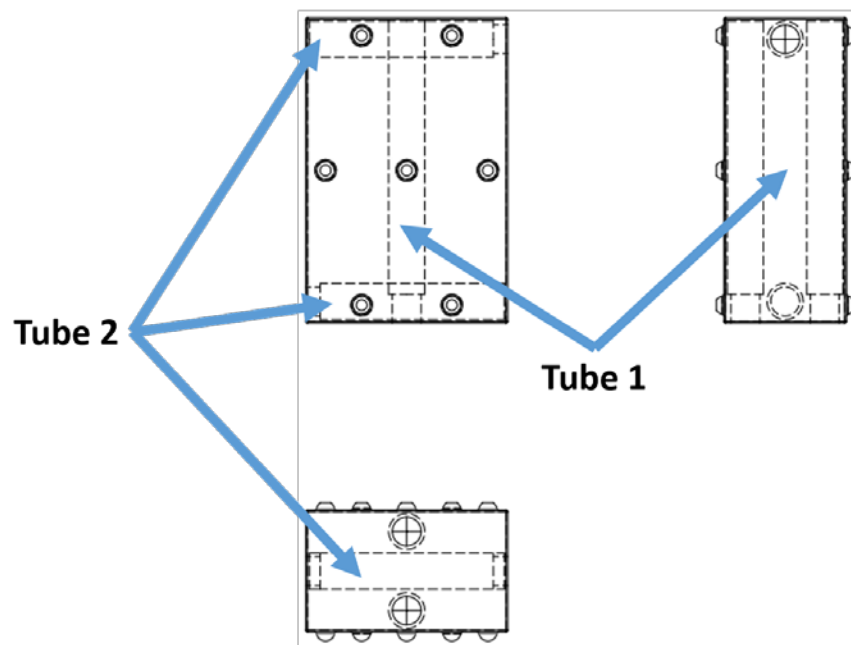
Figure 1. 3D view of the micro-swimmer

When tubes are activated under acoustic wave with certain frequency, tube 1 will produce a forward force and result in a translational movement. Tube 2s produce torque and result in a rotational movement.

3.1   MODEL SPECIFICATIONS

The micro-swimmer is made of IP-S photoresist, which is a novel product from NanoScribe (Nanoscribe GmbH, Germany), and fabricated by lithography 3D printing. The specifications of the micro-swimmer are illustrated in Table 2. Dimensions of the micro-swimmer are 950 μm × 460 μm × 340 μm. It is explicitly designed so that the density of the swimmer is slightly larger than water.

Table 2. Swimmer Specification

Parameters	Value
Length in m	9.5E-4
Width in m	4.6E-4
Height in m	3.4E-4
Average Density in kg/m^3	1.01E3
Tube Diameter in m	100E-6

It is noticeable that when acoustic wave with certain frequency is applied to the swimmer, bubbles in all tubes will oscillate but with distinct amplitude. Hence, movement in perpendicular direction may affect each other, and this phenomenon must be avoided. The tube length and selected frequency, given in Table 3, were picked after a number of trial and error experiments. The chosen values ensure that when one tube is activated, the bubble/bubbles in other tube/tubes do not oscillate large enough and result in a motion.

Table 3. Tube Lengths

	Length in m	Selected Frequency in Hz
Tube 1	8.6E-4	5300
Tube 2	3.8E-4	8300

3.2   MATHEMATICAL MODEL

The schematic diagram of the micro-swimmer is illustrated in Figure 2. A Cartesian coordinate is established with X representing the positive horizontal direction and Y representing the positive vertical direction. Ψ denotes the angular position and counter-clock wise is defined as the positive direction.

The kinematic equations of motion of the center of mass (COM) for the swimmer can be written as follows:

$$\dot{\chi}(t) = S(\chi)v,\qquad(3.2.1)$$

where the triplet $\dot{\chi}(t) = \begin{bmatrix} \dot{x}(t) & \dot{y}(t) & \dot{\varphi}(t) \end{bmatrix}^{T}$ is the time derivative of

$\chi(t) = \begin{bmatrix} x(t) & y(t) & \varphi(t) \end{bmatrix}^{T}$. $x(t)$ and $y(t)$ represent the position of the COM of the swimmer,

$\varphi(t)$ denotes the angular position of the swimmer, $S(\chi) \in R^{3\times3}$ is the transformation matrix

defined as follows:

$$S(\chi) = \begin{bmatrix} \cos\varphi & -\sin\varphi & 0 \\ \sin\varphi & \cos\varphi & 0 \\ 0 & 0 & 1 \end{bmatrix},\qquad(3.2.2)$$

and $v = \begin{bmatrix} v_1 & v_2 & v_3 \end{bmatrix}^{T}$ is the velocity vector. v_1, v_2 and v_3 denote the surge, sway, and yaw

velocities of the swimmer. The full dynamics can be expressed as

$$M\dot{v} = \tau_0 - D(v)v - F_{fr},\qquad(3.2.3)$$

where $\dot{v}(t)$ denotes the time derivative of $v(t)$. $M \in R^{3\times3}$ is the inertial matrix, which is defined

as

$$M = \begin{bmatrix} m & 0 & 0 \\ 0 & m & 0 \\ 0 & 0 & I_0 \end{bmatrix},\qquad(3.2.4)$$

where m, I_0 represent the mass and inertia of the swimmer, respectively. $D \in R^{3\times3}$ is the matrix

containing Centripetal–Coriolis and hydrodynamic terms, and is defined as

$$D(v) = \begin{bmatrix} Xv_1 & 0 & -mv_2 \\ 0 & Yv_2 & mv_1 \\ mv_2 & -mv_1 & Nv_3 \end{bmatrix},\qquad(3.2.5)$$

16

Xv_1, Yv_2, Nv_3 denote scalar, constant fluid drag coefficients and they are calculated in section 4.1.2.1. $F_{fr} \in R^{3\times1}$ represents the friction force from the contact surface, and is defined as

$$F_{fr} = \begin{bmatrix} F_{fr1}sign(v_1) \\ F_{fr2}sign(v_2) \\ F_{fr3}sign(v_3) \end{bmatrix}, \qquad (3.2.6)$$
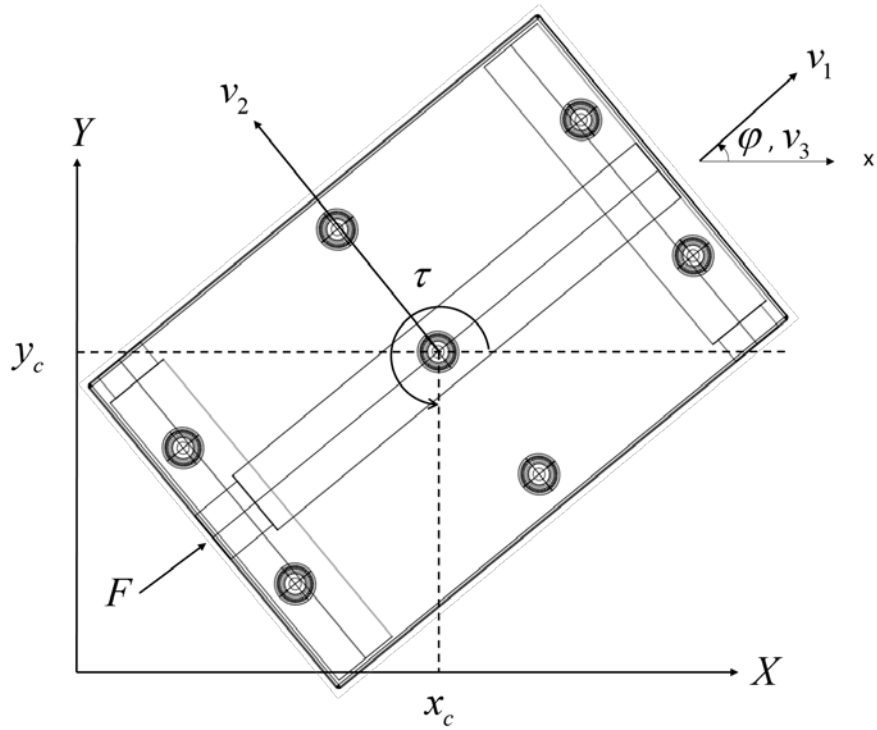

Figure 2. Schematic diagram of the micro-swimmer

where F_{fr1}, F_{fr2}, F_{fr3} are scalar friction forces in opposite direction to the velocities. The force–torque control input vector denoted by τ_0 is defined as

$$\tau_0 = \begin{bmatrix} F \\ 0 \\ \tau \end{bmatrix}, \tag{3.2.7}$$

where F denotes a control force that is applied to produce forward thrust and τ denotes a torque which is applied on the COM.

A significant feature of the micro-swimmer model is that the generalized propulsion forces are bidirectional while the amplitude and frequency cannot be negative, a simple switch was established and combined into the dynamics. It is explicitly defined as follows

$$\begin{bmatrix} F \\ \tau \end{bmatrix} = \mathcal{T}_m(\mathcal{O}) \begin{bmatrix} Amp_1 \\ Amp_2 \end{bmatrix} \tag{3.2.8}$$

where $\mathcal{T}_m(\mathcal{O}) \in R^{2\times2}$ is a transformation matrix and it is defined as

$$\mathcal{T}_m(\mathcal{O}) = \begin{bmatrix} \dfrac{1+sign(\mathcal{O}_1)}{2} & -\dfrac{1-sign(\mathcal{O}_1)}{2} \\ \dfrac{1+sign(\mathcal{O}_2)}{2} & -\dfrac{1-sign(\mathcal{O}_2)}{2} \end{bmatrix} \tag{3.2.9}$$

where $\mathcal{O}_i$, $i=1,2$ is a scalar index which related to the control signal. The amplitude $Amp \in \mathbf{R}^+$ and frequency $f_p \in \mathbf{R}^+$ of the bubble oscillation are two factors that affect the magnitude of the propulsion forces. It is fully modeled in [3] and can be written as

$$F_i = 0.8\rho \mathbf{A}_t (Amp_i f_{p_i})^2 \tag{3.2.10}$$

where $i=1-4$, $\rho \in \mathbf{R}^+$ is the density of the liquid and $\mathbf{A}_t \in \mathbf{R}^+$ is the cross-sectional area of the micro-tube. The resonant frequency of a gas bubble trapped in a micro-tube is related to the length of the tube. Each tube on the micro-swimmer has a distinct length to have a different resonant frequency f_{p_i}. In this acoustic forced vibration model, the bubble oscillation frequency

f_{p_i} is the same as the frequency of the sound wave. And for a fixed frequency, the bubble oscillation amplitude Amp_i is related to the amplitude of the sound wave and liquid medium. Details of amplitude relation can be found in section 3.1.

4.0   STATE ESTIMATION

This chapter focused on developing a State Dependent Coefficient (SDC) based estimator. An open-loop experiment was carried out. During the experiment, both ultrasound machine and camera images were collected. Camera data was utilized to do the system identification and the system model was verified by comparison of simulation and experiment trajectory. The SDC estimator was applied to 1) estimate measured data from ultrasound image to obtain more accurate information; 2) evaluate angular position and velocity which are unavailable from ultrasound image. The estimation results were compared with data from camera and a dynamic based Extended Kalman Filter (EKF).
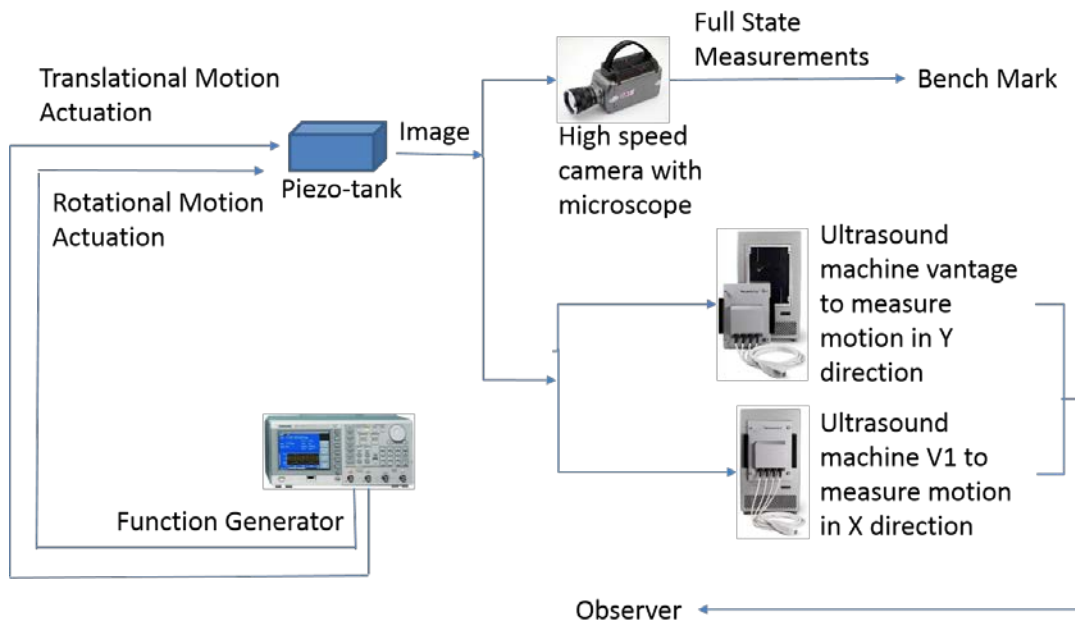

Figure 3 Experiment Process Flow Chart

4.1   EXPERIMENTS

This section reviews and analyzes the performed experiments. A prototype micro-swimmer, which has the same specification as mentioned in section 3.1, was used to carry out the experiment. The swimmer was driven by a pre-designed periodic acoustic wave combination and was expected to perform a circular movement. Both camera and ultrasound machine were applied to capture the movement of the swimmer. The details of the process is illustrated in Figure 3.

4.1.1   Experimental Implementation

The experiment setup is illustrated in Figure 4. The swimmer was placed on a glass plate and the latter one was attached on a water tank bottom. Two piezo-vibrators were attached to two adjacent side walls of the water tank. These piezo-vibrators produce distinct acoustic waves. Two ultrasound transducers were placed perpendicular to each other and they were both set at an angle of 30 degrees with respect to the water surface. The camera was placed vertically to the water surface.
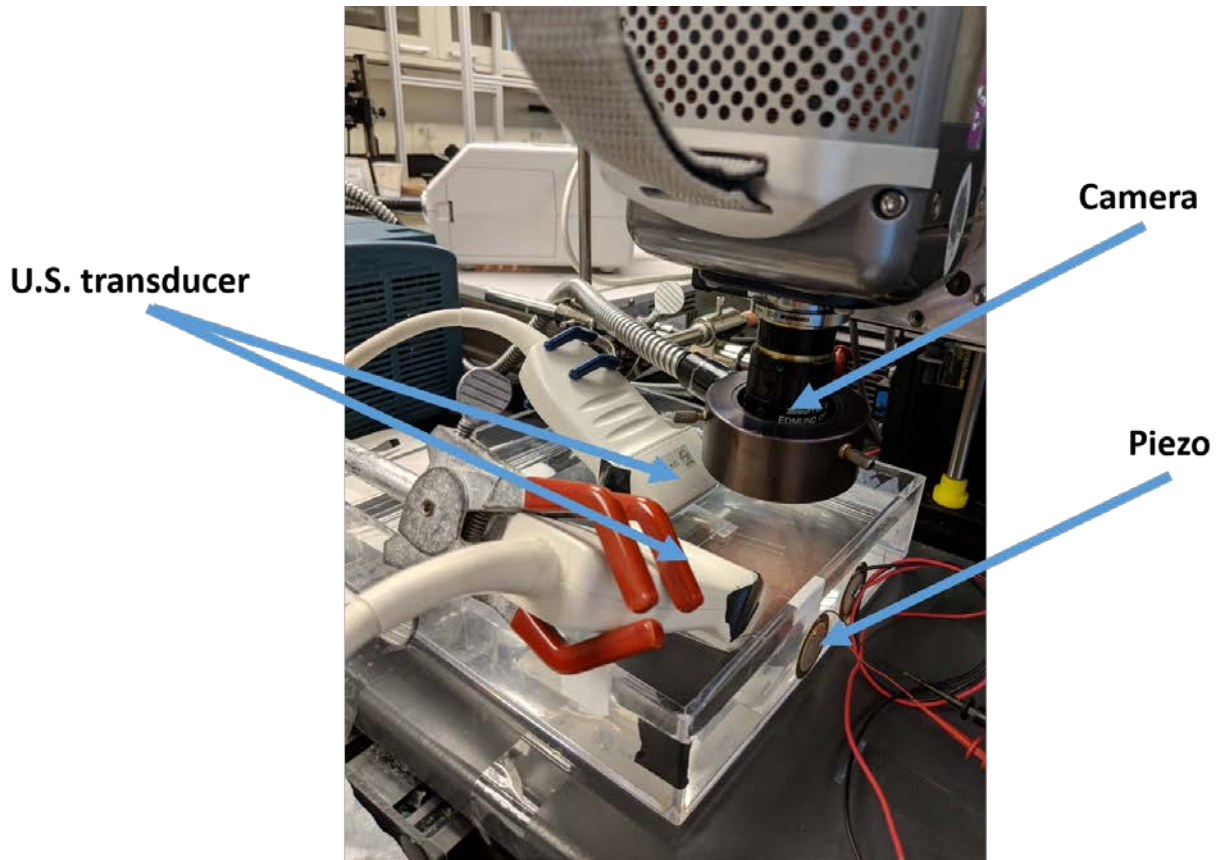
Figure 4 Experiment setup

One function generator and one amplifier were implemented to generate periodic electrical waveforms. The voltage was enlarged 110 times by the amplifier and sent to the piezo-vibrators. Two electrical waveforms in different frequencies were produced by separate channels on the function generator. The pre-defined periodic acoustic wave combination was calculated upon the (Figure 5) measured relationship between the voltage of the function generator signal and the amplitude of the bubble oscillation. The frequencies were fixed as $5300Hz$ for tube 1 (translational motion) and $8300Hz$ for tube 2 (rotational motion).
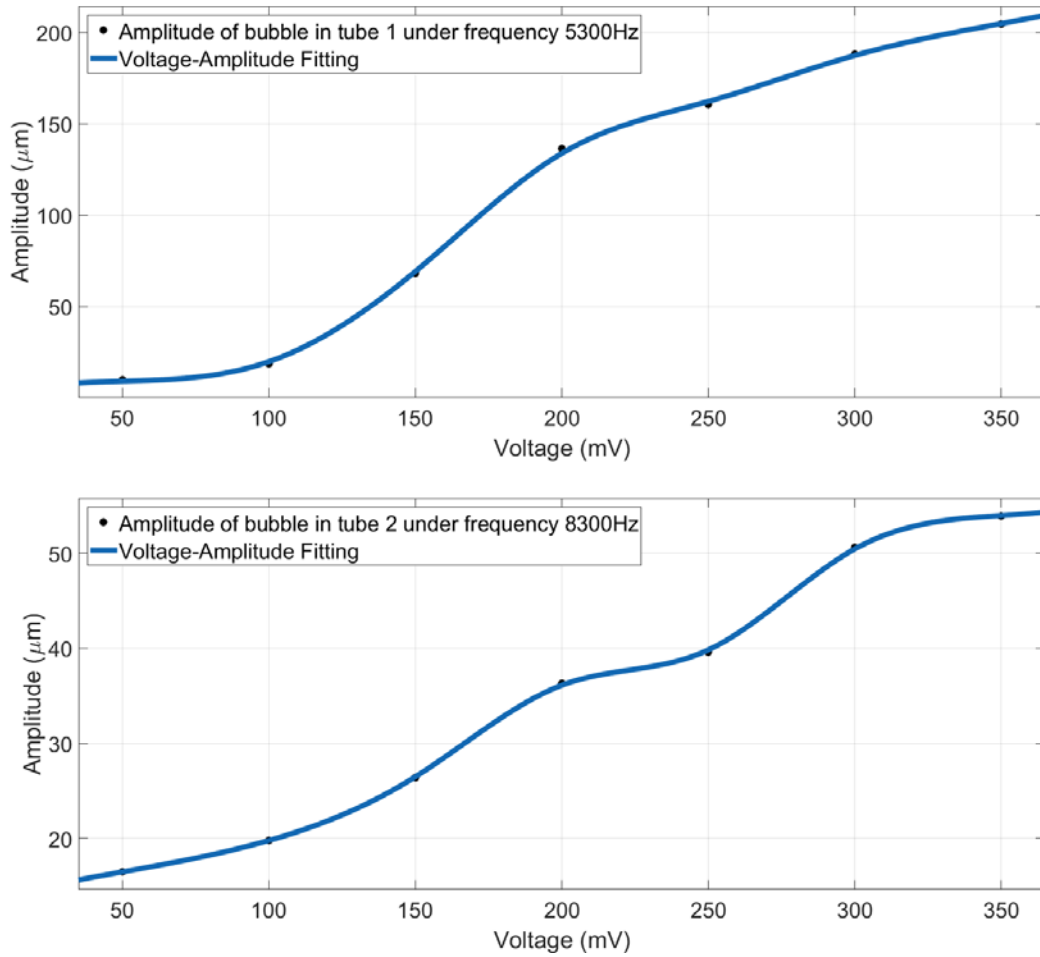
Figure 5 Amplitude and voltage relation

The camera was set to capture the images in the resolution of 656×656 for 60 frames per second (FPS). And the field of view (FOV) was $6.16mm \times 6.16mm$. Each ultrasound transducer was set to have a FOV of $32.4mm \times 7.29mm$. As a consequence the intersection area of these two transducers was $7.29mm \times 7.29mm$ (Figure 6). The ultrasound image recording was limited to 30 FPS because of buffer size restriction.

During the experiment, the swimmer was always set to start can complete a movement within the FOV of both camera and ultrasound transducer. All translational movements and

rotational movement of the swimmer were recorded by the camera. Each ultrasound transducer captured one of the two translational movements.
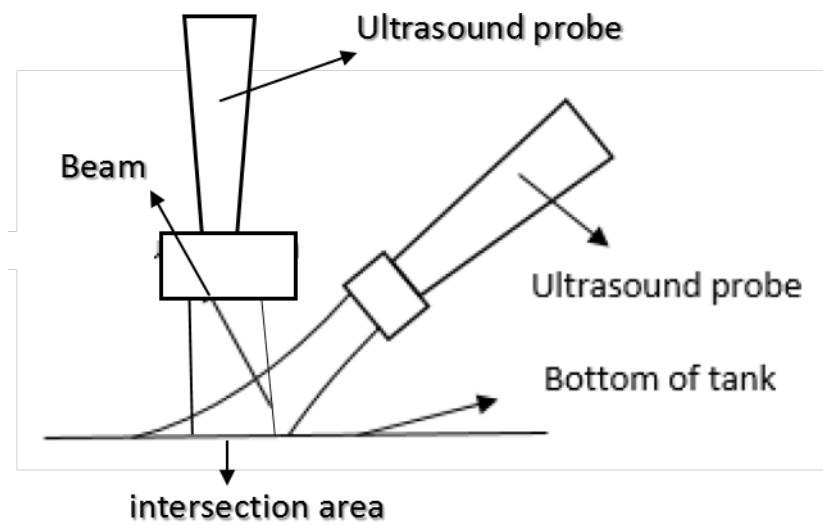
Figure 6 Ultrasound transducer setup

4.1.2   System Identification

System identification (System ID) uses experiment data to calculate the unknown system parameters mentioned in section 3.2. In this case, camera data was used as the bench mark and is utilized to complete the System ID. The captured image of the micro-swimmer during movement is shown in Figure 7

Figure 7 Micro-swimmer images captured in experiment. (a) Camera images of the micro-swimmer. (b) Ultrasound image of the micro-swimmer moving in Y direction. (c) Ultrasound image of micro-swimmer moving in X direction. (d) Plot of movement during experiment.

4.1.2.1 Fluid Damping Force

Drag force for a small object in a laminar flow is described by Stokes' law. However, the swimmer has a shape of a cuboid. Hence, the Navier-Stokes equations might not be accurate when the object shape factor is not considered. D. Leith [30] suggested that drag force can be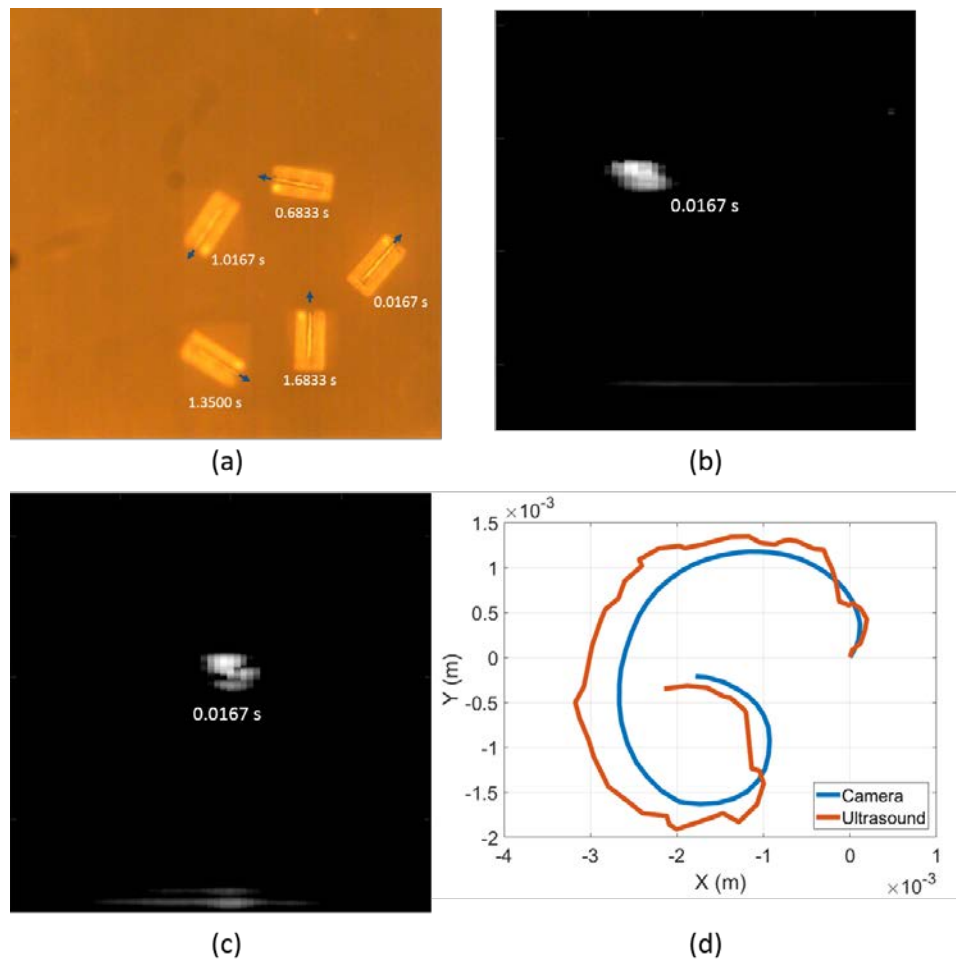 expressed through the diameter of sphere with equal projected area normal to its velocity direction and effective surface as

$$F_D = 3\pi\mu V \left[\frac{1}{3}d_n + \frac{2}{3}d_s \right],$$

(4.1.1)

where μ is the dynamic viscosity, V is the flow velocity relative to the object, d_s is the diameter of sphere whose effective surface equals that of the object and d_n is the diameter of sphere whose projected area equals that of the object projected normal to its direction of velocity.

Since the drag force is in proportional relationship with velocity, the coefficients in eq. (3.2.5) can be defined as

$$X_{v1} = 3\pi\mu_1 \left[\frac{1}{3}d_{n1} + \frac{2}{3}d_{s1} \right]$$

(4.1.2)

$$Y_{v2} = 3\pi\mu_2 \left[\frac{1}{3}d_{n2} + \frac{2}{3}d_{s2} \right]$$

(4.1.3)

$$N_{v3} = 3\pi\mu_3 \left[\frac{1}{3}d_{n3} + \frac{2}{3}d_{s3} \right]$$

(4.1.4)

The calculated coefficients are shown in Table 4.

Table 4 Fluid Damping Force Coefficients

Parameters	Value
X_{v1}	1.3118E-6
Y_{v2}	4.5913E-6
N_{v3}	1.1918E-8

4.1.2.2 Slide Friction

In *macrotribology*, the friction force is in linear proportion to the normal force between two contact surfaces. The friction coefficient is determined by physical features of the two surfaces. While micro-scale friction force has multiple influence factors. Factors include adhesive forces, capillary forces, contact elasticity, topography, surface chemistry, and generation of a third body, etc. [31]. Any of them can dominate in specific circumstances. According to [32], the friction force can be expressed as

$$F_{fr} = S\pi(RN/K)^{\frac{2}{3}}$$ (4.1.5)

where N is the normal contact force, S is the shear stress of the asperity junction, R is the asperities reduced radii of curvature, and K is the reduced Young's moduli of the two interacting asperities. Nevertheless, in this swimmer case, above parameters are not easy to determine. Further, some studies still apply macro-scale equation to model micro-scale case, e.g. [33]. Due to aforementioned reasons, the friction force of the micro-swimmer will be kept in linear form. More accurate friction model will be experimentally identified in future study.

The friction force can be calculated by solving eq. (3.2.3) and the result is shown in Figure 8. It is noticeable that friction force is not constant during the experiment. One of the reasons is that the glass plate surface is not perfectly plat. Another reason is because the micro-swimmer is not perfectly symmetric. Two parallel tubes will produce a torque which, as a consequence, increases the normal force.
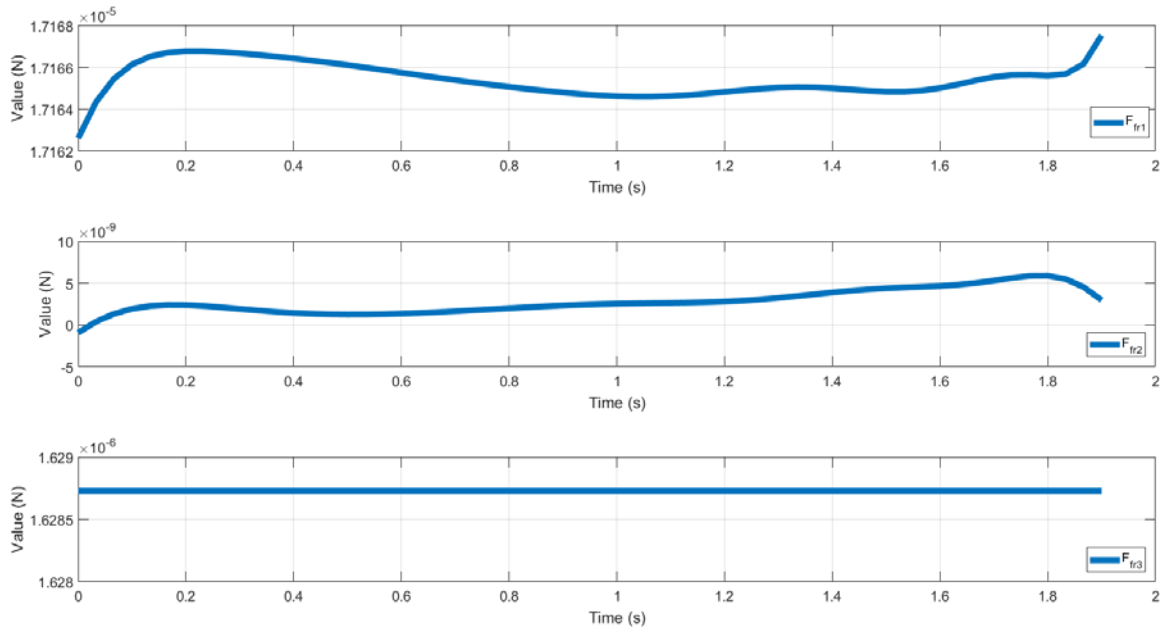

Figure 8 Calculated friction from experiment data

In this case, the friction force is approximated and will be kept constant for later study. The values of μ_i are given in Table 5 and they will be used for estimator and controller development.

Table 5 Friction force during the experiment

Parameters	Value
μ_1	1.7165E-5
μ_2	2.7767E-9
μ_3	1.6287E-6

4.2 DYNAMIC AND MEASUREMENT MODEL

The state space form of (3.2.3) is derived by the following

$$\dot{q} = f(q, u), \tag{4.2.1}$$

where

$$\dot{q} = \begin{bmatrix} \dot{q}_1 & \dot{q}_2 & \dot{q}_3 & \dot{q}_4 & \dot{q}_5 & \dot{q}_6 \end{bmatrix}^T \tag{4.2.2}$$

and

$$f(q, u) = \begin{bmatrix} q_2 & \lambda_{x1} & q_4 & \lambda_{x2} & q_6 & (\tau - N_{v3} q_6) \dfrac{1}{I_0} \end{bmatrix}^T \tag{4.2.3}$$

where

$$\lambda_{x1} = \left(F \cos q_5 + \mu_1 \cos q_5 + \mu_2 \sin q_5 - X_{v1} q_2 (\sin q_5)^2 - \frac{1}{2} X_{v1} q_4 \sin 2q_5 - Y_{v2} q_2 (\sin q_5)^2 + \frac{1}{2} Y_{v2} q_4 \sin 2q_5 \right) \frac{1}{m}$$

29

$$\lambda_{x2} = \left(F\sin q_5 + \mu_1 \sin q_5 - \mu_2 \cos q_5 - Y_{v2} q_4 (\sin q_5)^2 - \frac{1}{2} X_{v1} q_2 \sin 2q_5 - X_{v1} q_4 (\sin q_5)^2 + \frac{1}{2} Y_{v2} q_2 \sin 2q_5 \right) \frac{1}{m}$$

The extended linear form of the dynamic system (4.2.1) for state estimation can be written as

$$\dot{q} = \overline{A}(q)q + Bu + \omega \tag{4.2.4}$$

where, $\overline{A}(q)q + Bu = f(q,u)$, $\omega \in \mathbf{R}^{6 \times 1}$ is the process noise characterized by zero-mean Gaussian process and associated with the process noise covariance matrix $Q \in \mathbf{R}^{3 \times 3}$.

The measurement model is given as follows

$$\begin{aligned} Z &= h(\chi) + v \\ &= \begin{bmatrix} x & \dot{x} & y & \dot{y} \end{bmatrix}^T + v \end{aligned} \tag{4.2.5}$$

where $v \in \mathbf{R}^2$ is a zero-mean Gaussian measurement noise with the measurement covariance matrix $S \in \mathbf{R}^{4 \times 4}$.

4.3   SDC PARAMETERIZATION

$\overline{A}(q) \in \mathbf{R}^{6 \times 6}$ can be expressed as a convex combination:

$$\overline{A}(q)q = \rho_1 A_1(q)q + ... + \rho_5 A_5(q)q \tag{4.3.1}$$

where $\rho_1, ..., \rho_5 \geq 0$ and $\sum_{i=1}^{5} \rho_i = 1$ where ρ_i represents the weights assigned to each SDC parameter. The matrices A_i (for $i = 1 - 5$) are given below

$$A_1 = \begin{bmatrix} 0 & 1 & 0 & 0 & 0 & 0 \\ 0 & C_{q21} & 0 & C_{q41} & 0 & 0 \\ 0 & 0 & 0 & 1 & 0 & 0 \\ 0 & C_{q22} & 0 & C_{q42} & 0 & 0 \\ 0 & 0 & 0 & 0 & 0 & 1 \\ 0 & 0 & 0 & 0 & 0 & -\dfrac{N_{v3}}{I_0} \end{bmatrix} \tag{4.3.2}$$

$$A_2 = \begin{bmatrix} 0 & 1 & 0 & 0 & 0 & 0 \\ 0 & 0 & 0 & C_{q41} & \dfrac{C_{q21}\hat{q}_2}{\hat{q}_5} & 0 \\ 0 & 0 & 0 & 1 & 0 & 0 \\ 0 & C_{q22} & 0 & C_{q42} & 0 & 0 \\ 0 & 0 & 0 & 0 & 0 & 1 \\ 0 & 0 & 0 & 0 & 0 & -\dfrac{N_{v3}}{I_0} \end{bmatrix} \tag{4.3.3}$$

$$A_3 = \begin{bmatrix} 0 & 1 & 0 & 0 & 0 & 0 \\ 0 & C_{q21} & 0 & 0 & \dfrac{C_{q41}\hat{q}_4}{\hat{q}_5} & 0 \\ 0 & 0 & 0 & 1 & 0 & 0 \\ 0 & C_{q22} & 0 & C_{q42} & 0 & 0 \\ 0 & 0 & 0 & 0 & 0 & 1 \\ 0 & 0 & 0 & 0 & 0 & -\dfrac{N_{v3}}{I_0} \end{bmatrix} \tag{4.3.4}$$

$$A_4 = \begin{bmatrix} 0 & 1 & 0 & 0 & 0 & 0 \\ 0 & C_{q21} & 0 & C_{q41} & 0 & 0 \\ 0 & 0 & 0 & 1 & 0 & 0 \\ 0 & C_{q22} & 0 & 0 & \dfrac{C_{q42}\hat{q}_4}{\hat{q}_5} & 0 \\ 0 & 0 & 0 & 0 & 0 & 1 \\ 0 & 0 & 0 & 0 & 0 & -\dfrac{N_{v3}}{I_0} \end{bmatrix} \tag{4.3.5}$$

31

$$
A_5 = \begin{bmatrix}
0 & 1 & 0 & 0 & 0 & 0 \\
0 & C_{q21} & 0 & C_{q41} & 0 & 0 \\
0 & 0 & 0 & 1 & 0 & 0 \\
0 & 0 & 0 & C_{q42} & \dfrac{C_{q22}\hat{q}_2}{\hat{q}_5} & 0 \\
0 & 0 & 0 & 0 & 0 & 1 \\
0 & 0 & 0 & 0 & 0 & -\dfrac{N_{v3}}{I_0}
\end{bmatrix}
\tag{4.3.6}
$$

where

$$
C_{q21} = \left(-X_{v1}\left(\cos\hat{q}_5 \right)^2 + Y_{v2}\left(\sin\hat{q}_5 \right)^2 \right)\frac{1}{m},
$$

$$
C_{q41} = \left(X_{v1}\sin 2\hat{q}_5 + Y_{v2}\sin 2\hat{q}_5 \right)\frac{1}{2m},
$$

$$
C_{q22} = \left(X_{v1}\sin 2\hat{q}_5 + Y_{v2}\sin 2\hat{q}_5 \right)\frac{1}{2m},
$$

$$
C_{q42} = \left(X_{v1}\left(\sin\hat{q}_5 \right)^2 - Y_{v2}\left(\cos\hat{q}_5 \right)^2 \right)\frac{1}{m}.
$$

The measurement model can be parameterized as

$$
Z = \bar{C}(q)q + v
\tag{4.3.7}
$$

where $\bar{C}(q) \in \mathbf{R}^{4\times 6}$ is the output matrix and $\bar{C}(q)q = h(\chi)$. It can be expressed as:

$$
\bar{C} = \begin{bmatrix}
1 & 0 & 0 & 0 & 0 & 0 \\
0 & 1 & 0 & 0 & 0 & 0 \\
0 & 0 & 1 & 0 & 0 & 0 \\
0 & 0 & 0 & 1 & 0 & 0
\end{bmatrix}
\tag{4.3.8}
$$

The SDC based estimator is given by

$$
\dot{\hat{q}} = f(\hat{q},u) + K(\hat{q},t)(Z - h(\hat{\chi}))
\tag{4.3.9}
$$

32

$$K(\hat{q},t) = P(t)\overline{C}^T S^{-1} \tag{4.3.10}$$

where $P(t) \in \mathbf{R}^{6 \times 6}$ represents the propagated error covariance matrix and is obtained by solving the algebraic Riccati equation

$$\overline{A}^T (q)P + P\overline{A}(q) + 2\alpha P - 2P(\overline{C}^T (q)S^{-1}\overline{C}(q))P + Q = 0 \tag{4.3.11}$$

4.4   ESTIMATION RESULTS

This section shows the estimation results. Overall, it is clear that data collected from ultrasound image has a large error from that of camera. Velocity data is calculated by differentiating position data from either camera or ultrasound image. Because of the low frame rate of ultrasound machine, the velocity measurements vary significantly. Despite poor measurements, SDC provides accurate position and velocity estimation. Further, the unmeasurable rotational information of ultrasound image is evaluated and compared to that of camera image. An optimization procedure was done by using MATLAB 'fmincon' function. The optimized weights of the SDC parameterization in eq. (4.3.1) are given in Table 6.

Table 6 Optimized SDC parameter weight

Weight	ρ_1	ρ_2	ρ_3	ρ_4	ρ_5
Value	0.0004	0.5986	0.0006	0.3999	0.0005

Figure 9 presents one of captured motions from experiment and associated estimation results. The camera captured data (blue line in the figure), which is same in section 4.1.2, is utilized as a bench mark. A simulation result is plotted as the red line in Figure 9. It is built upon the System ID in aforementioned section. The plot shows the simulated trajectory fits bench mark trajectory (the red line fits the blue line) and, therefore, verifies the correctness of System ID. However, the approximation of friction force causes minor error and as a consequence affects the estimation results. The yellow line in Figure 9 represents the measurement from ultrasound image. The SDC and EKF estimated positions are represented in purple line and green line respectively.
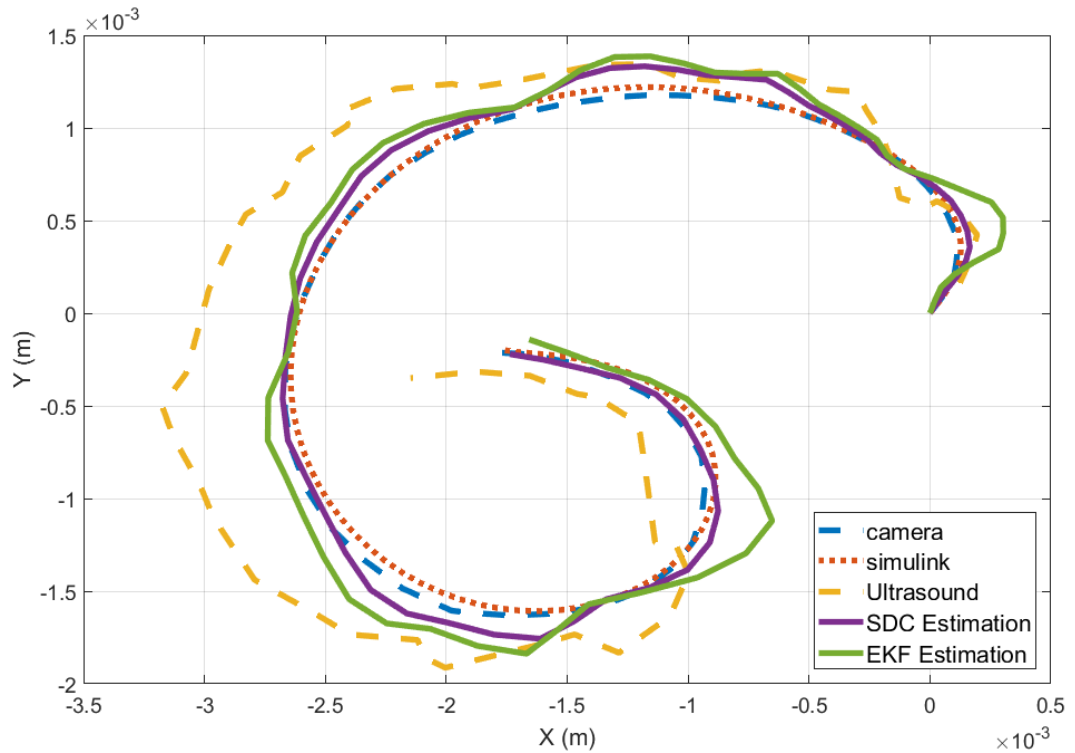

Figure 9 Estimation Results

The measurement and estimation errors are normalized with respect to the swimmer width and illustrated in Figure 10. It can be seen that both estimator provide state estimation and largely lower the error regards to the bench mark. Compared to EKF estimator, the estimation from SDC is more accurate than the EKF with an average of 22% normalized position estimation error. Further estimation results from SDC are presented in Figure 12 and Figure 13. It is noticeable that the estimated angular position (φ) and velocity fit the bench mark perfectly. This is because both SDC estimator and EKF are dynamic based so that they apply model predict value to correct the measurement drift. Since there is no angular measurements, the estimation of angular position and velocity equals those from model prediction. Nevertheless, minor estimation error still exists due to the approximation of System ID. The error is presented in Figure 11.
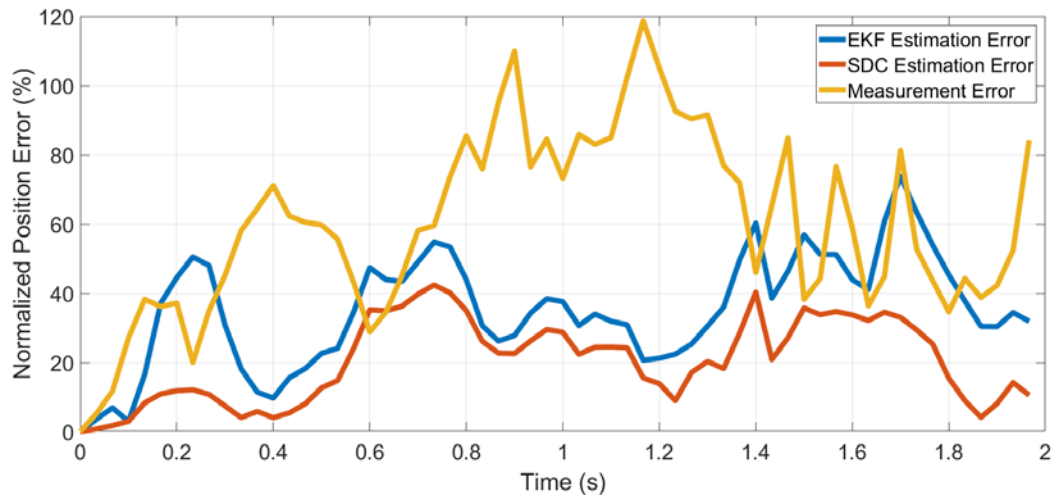

Figure 10 Normalized position estimation errors

The limitation of SDC estimator is that the weights of parameters need to be optimized to reduce the estimation error. The optimization procedure can only be done offline currently. Pre-optimization can solve part of the problem if the micro-swimmer is only working in pre-determined path/circumstances. In order to work in more universal cases, research for online optimization is required. Another limitation is the performance of estimator highly relied on the knowledge of the dynamic model. Section 3.1 shows that the friction force from the water tank bottom is not constant, this will be an unknown knowledge to the real-time experiment and the accuracy of estimation will be significantly affected.
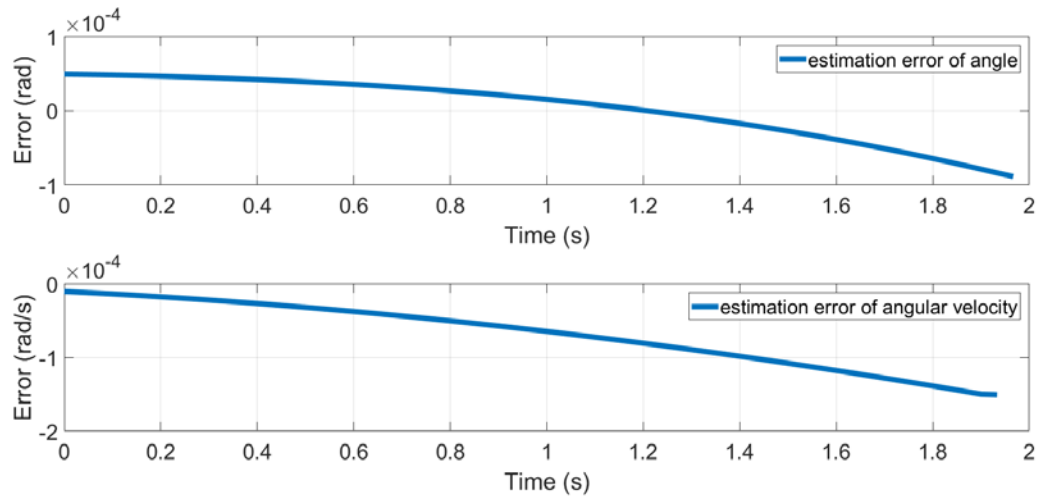

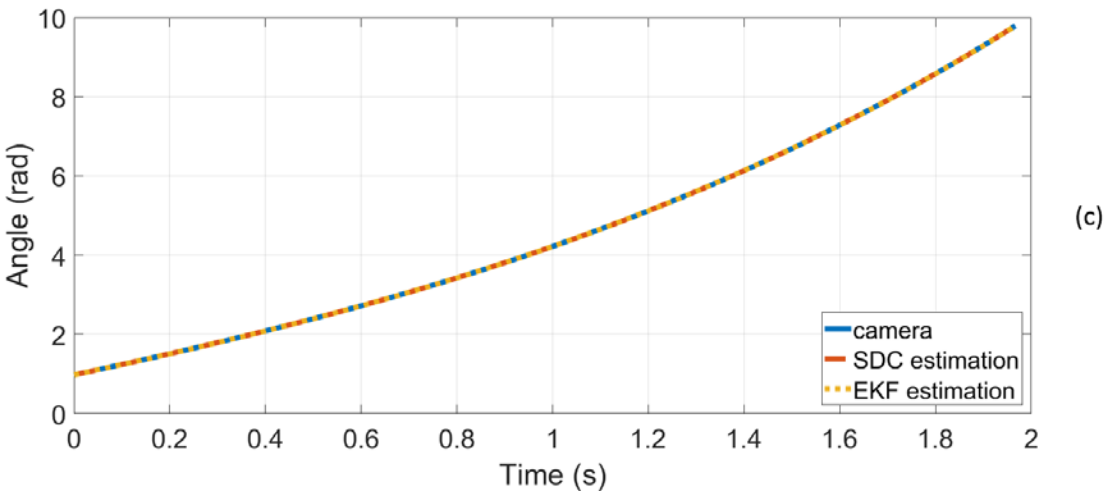**Figure 11** Estimation error of angular position and velocity
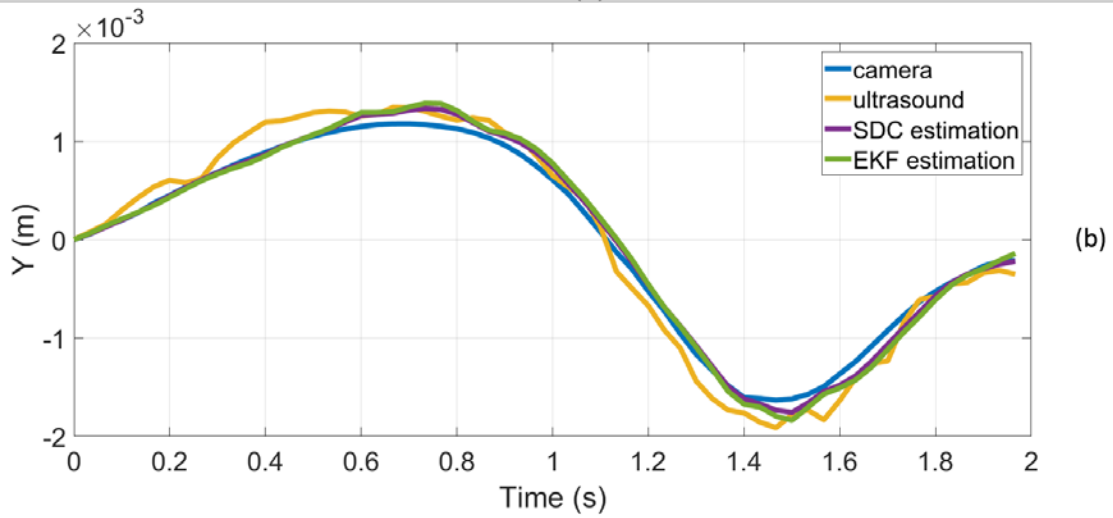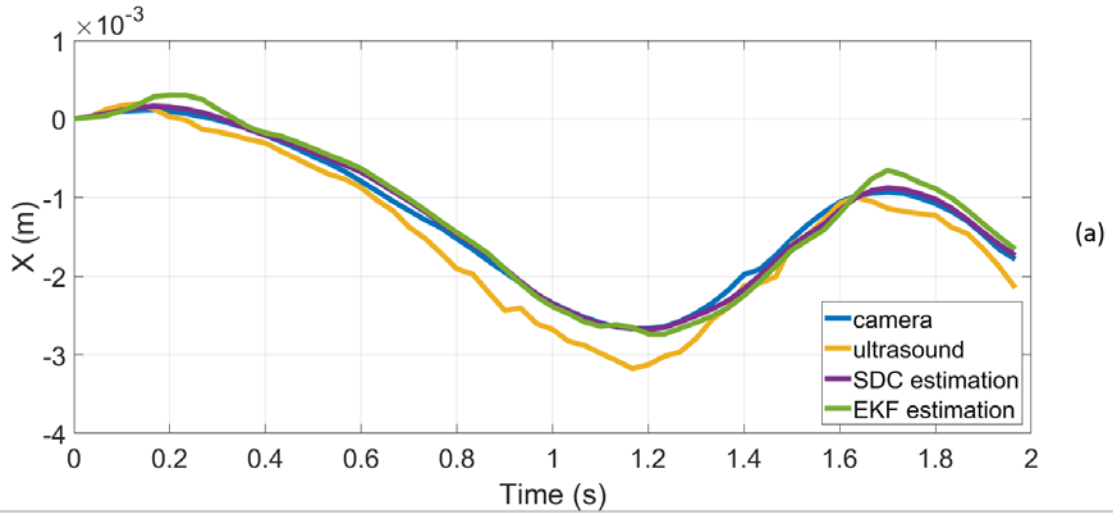
Figure 12 Estimated Position of SDC is compared to the bench mark and measurement from ultrasound image in this figure. (a) shows the position data in x direction; (b) gives the position data in y direction; (c) presents the estimated and bench mark angular position

Figure 13 This figure shows the comparison of bench mark, estimated and measured velocities. (a) gives the velocity data in x direction; (b) shows the velocity data in y direction; (c) presents the angular velocity estimation compared with bench mark data

5.0 CONTROL SYSTEM COUPLED WITH ESTIMATION

This section focuses on developing a feedback control strategy combined with SDC estimation. A control strategy based on [34] was modified to include the friction force mentioned in section 4.1.2.2. In this chapter, a simulation 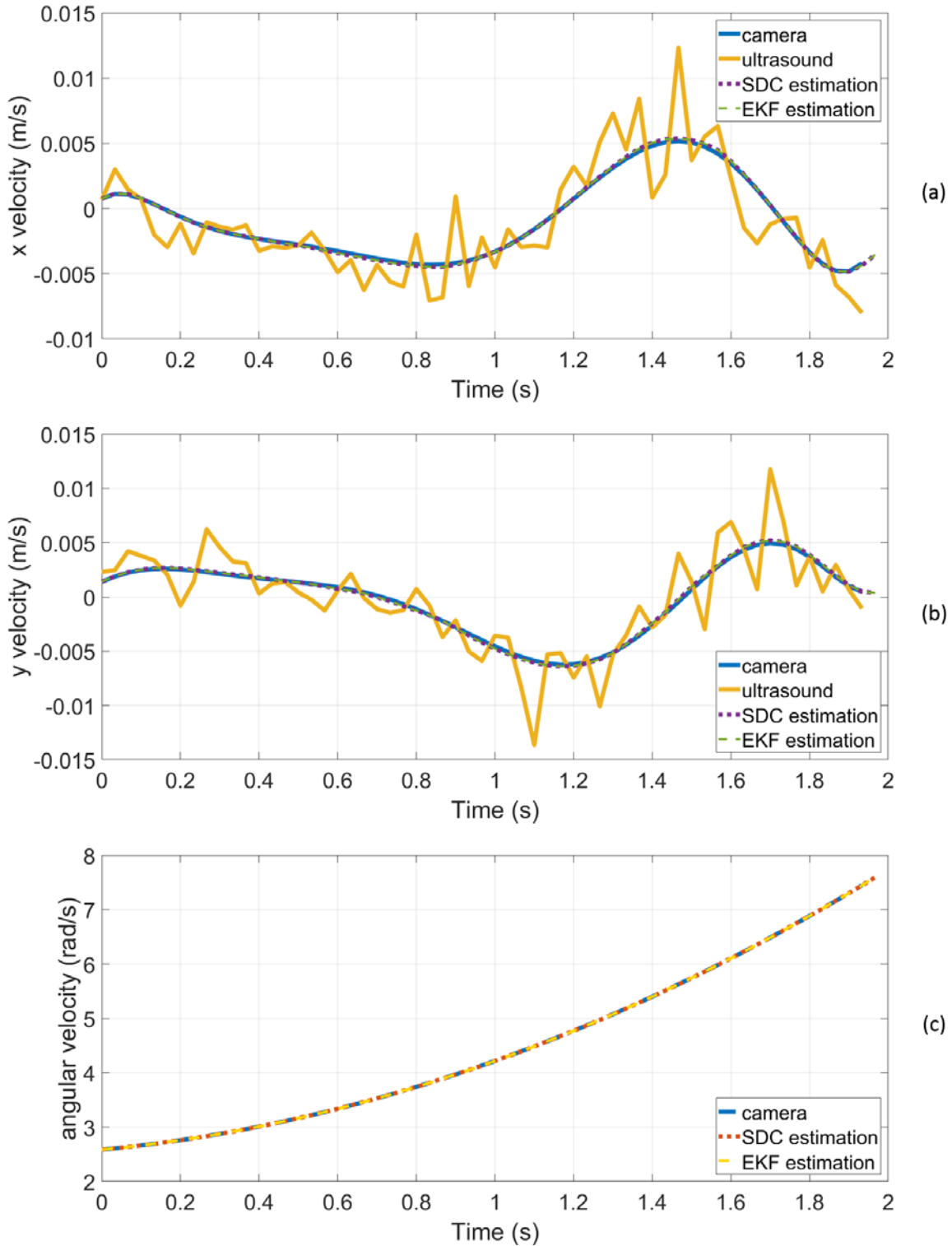model of the whole feedback control loop was built. Performance of the SDC coupled with controller was showed and discussed. A designed input switch mechanism was also demonstrate to produce bidirectional swimming motion from counteracting tubes that produce motion in only one direction.

5.1 CONTROL DEVELOPMENT

This section used a different swimmer, which has an additional set of tube to realize rotation to the other direction, from chapter 4.0 . The free body diagram is shown in Figure 14. There are three different tubes (differ in length) on the swimmer, each of them has unique oscillation frequency. Different colored arrow in Figure 14 represents tubes in different length. The blue arrow represents tube 1 and there are two of them placed in centrosymmetric position. When being activated, tube 1 will produce a torque in counter-clockwise direction. Similarly, activating tube 2 will result in clockwise rotation. Last, tube 3 is in charge of forward motion. It is not able to move backwards.
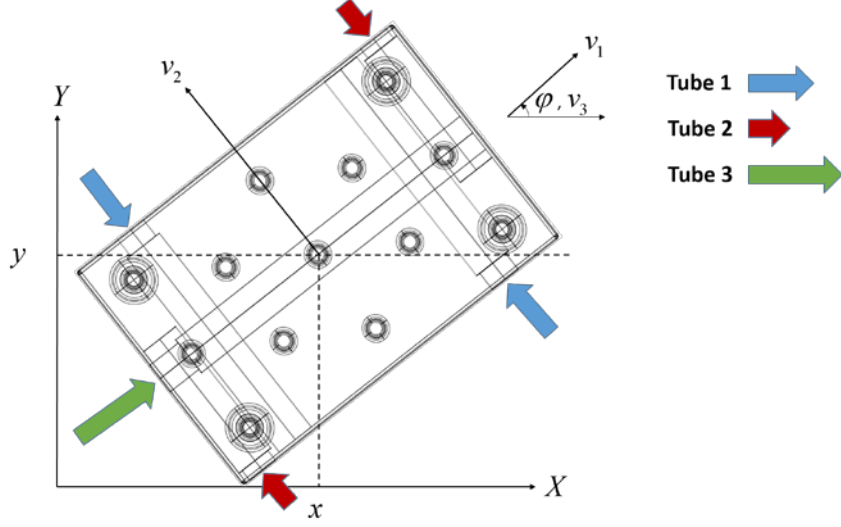
Figure 14 This figure illustrates the free body diagram

The control task to track some defined trajectory and reduce the tracking error to zero. Hence, define tracking errors as

$$\tilde{x} = x - x_{rc}, \ \tilde{y} = y - y_{rc}, \ \tilde{\varphi} = \varphi - \varphi_r \tag{5.1.1}$$

where x_{rc}, y_{rc}, φ_r are reference position and orientation.

The control law is developed upon the work in [34], and it can be expressed as

$$\tau_0 = \overline{\tau}_0 + F_{fr}, \tag{5.1.2}$$

where

$$\overline{\tau}_0 = \begin{bmatrix} \overline{F} & 0 & \overline{\tau} \end{bmatrix}^T, \tag{5.1.3}$$

where

$$\overline{F} = X_{v1}v_1 + m\overline{F}_1, \tag{5.1.4}$$

and

$$\overline{\tau} = N_{v3}v_3 + I_0\overline{\tau}_1, \tag{5.1.5}$$

40

where $\bar{F}_1$, $\bar{\tau}_1$ denote subsequently designed auxiliary control inputs. Details of control law and stability of the system is provided in the Appendix A.

5.2   SIMULATION

The main task of simulation is to 1) verify that the controller is still valid with additional friction term; 2) show that under the condition of unmeasurable state measurements, the controller is still valid with the assistant of estimator; 3) demonstrate how input switch works.

5.2.1   Simulation model

The simulation model was developed based on the control strategy mention in section 5.1, and the SDC estimator was built exactly same as described in section 4.0 The coefficients of dynamics were obtained from system identification mentioned in section 4.1.2. The simulation flow chart is shown in Figure 15. The simulation utilizes the ultrasound image as only feedback signal to the control system. Therefore, it is assumed that two out of six measurements are not able to obtain. Moreover, the step size of the simulation is fixed as $\frac{1}{30}$ since the frame rate of ultrasound machine during previous experiment is 30FPS.
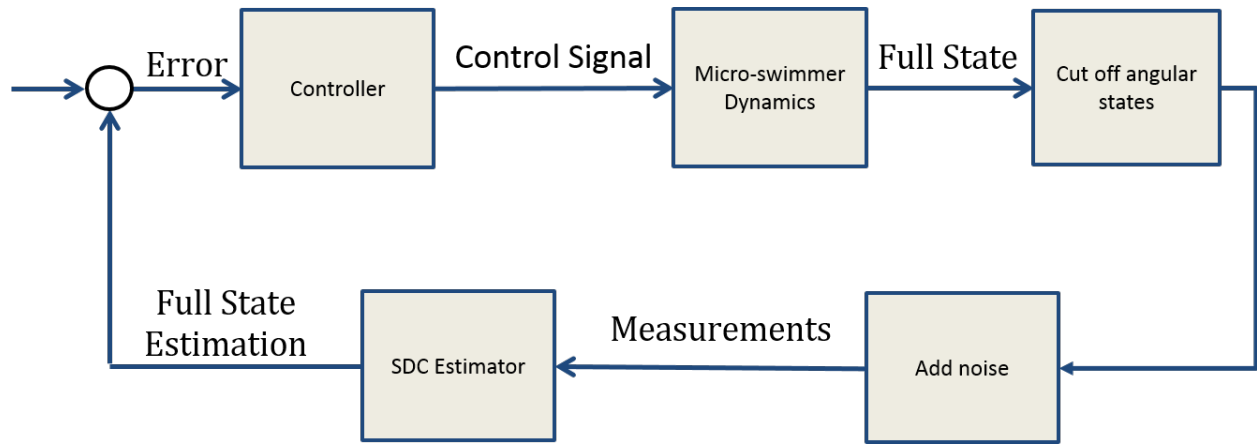
Figure 15. Control-estimator configuration during tests with ultrasound image tracking

5.2.2 Simulation Result

The simulation results in Figure 16 and Figure 17 show that the swimmer tracks an '8' reference trajectory for 14 seconds. It is clear that the swimmer follows the path with moderate tracking error. The results prove that even through the full state information is not available, an estimator can accurately evaluate the missing information. This implies that in a real-time close loop control experiment, even though the ultrasound image is not capable to provide the rotational information of the micro-swimmer, the controller will work by using the estimator.

The tracking error is caused by two major parts. First, the stability is proven to be globally uniformly ultimately bounded (GUUB). So the tracking error is expected to vary within the boundary. Second, the estimation error might increase the overall magnitude of tracking error. It is primarily caused by un-optimized SDC parameter weights. To improve performance, either pre-optimization or online optimization process to find parameterization weight is needed.

42
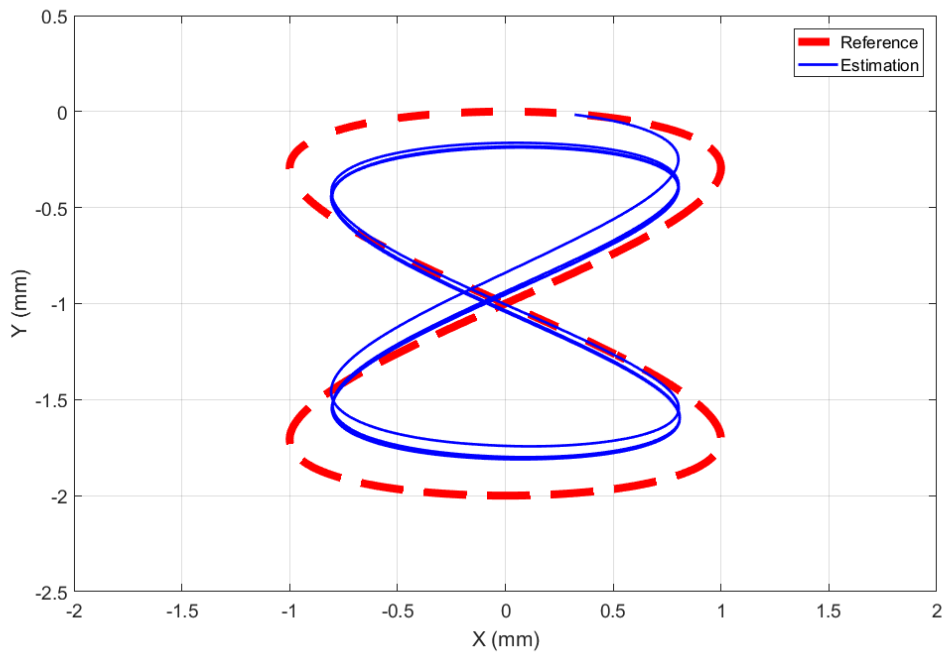
Figure 16 Simulation trajectory
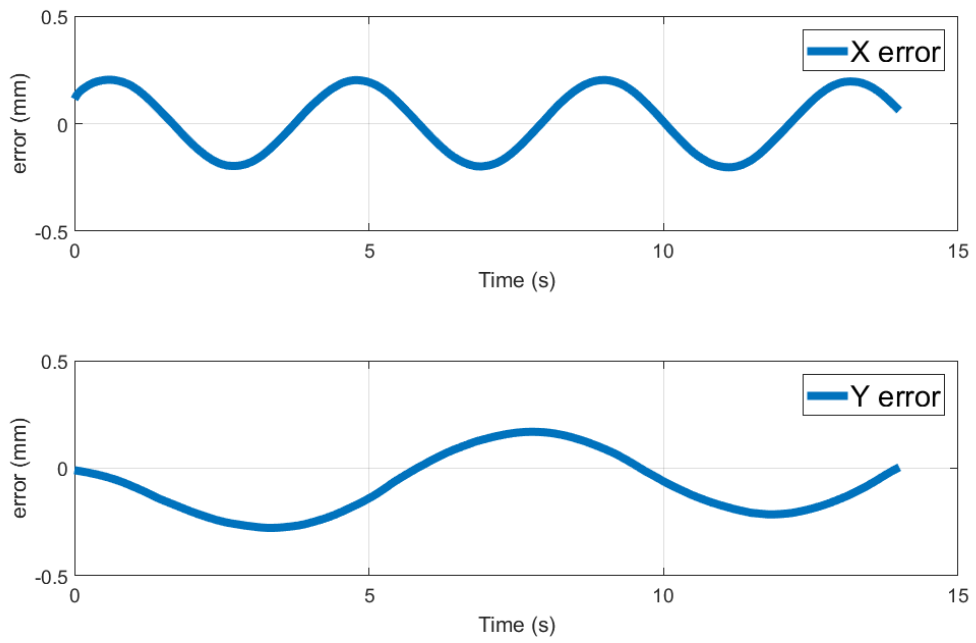
Figure 17 Simulation tracking error

Figure 19 demonstrates the input switch mechanism, mentioned in section 3.2, during the simulation. The switch signal $\mathcal{O}$ changes sign when channels on the opposite direction are required to be activated (Figure 18). For instance, when $sign(\mathcal{O}) = 1$, tube 1 will be activated, otherwise, tube 2 will be activated. It can be clearly seen from the figure that both control input $Amplitude_1$ (for tube 1) and $Amplitude_2$ (for tube 2) are always positive, while the general torque τ is bidirectional.

Figure 18 Input switch during a tracking task

Figure 19 This figure demonstrates the simulation input switch during the simulation (a) shows the required generalized torque value; (b) shows the switch signal changes sign with respect to the torque; (c) presents the amplitude of bubble oscillation when tube 1 is activated; (d) presents the amplitude of tube 2 when it is activated

6.0   CONCLUSION AND FUTURE WORKS

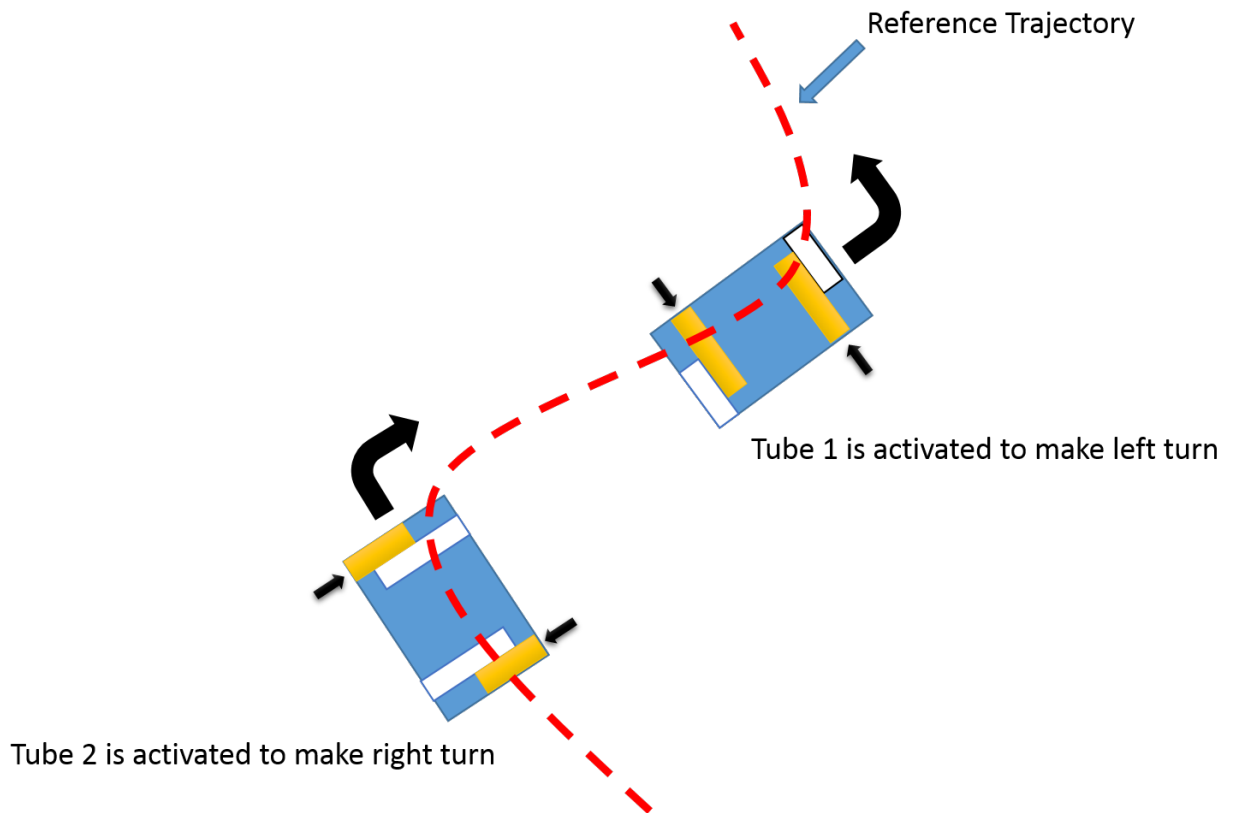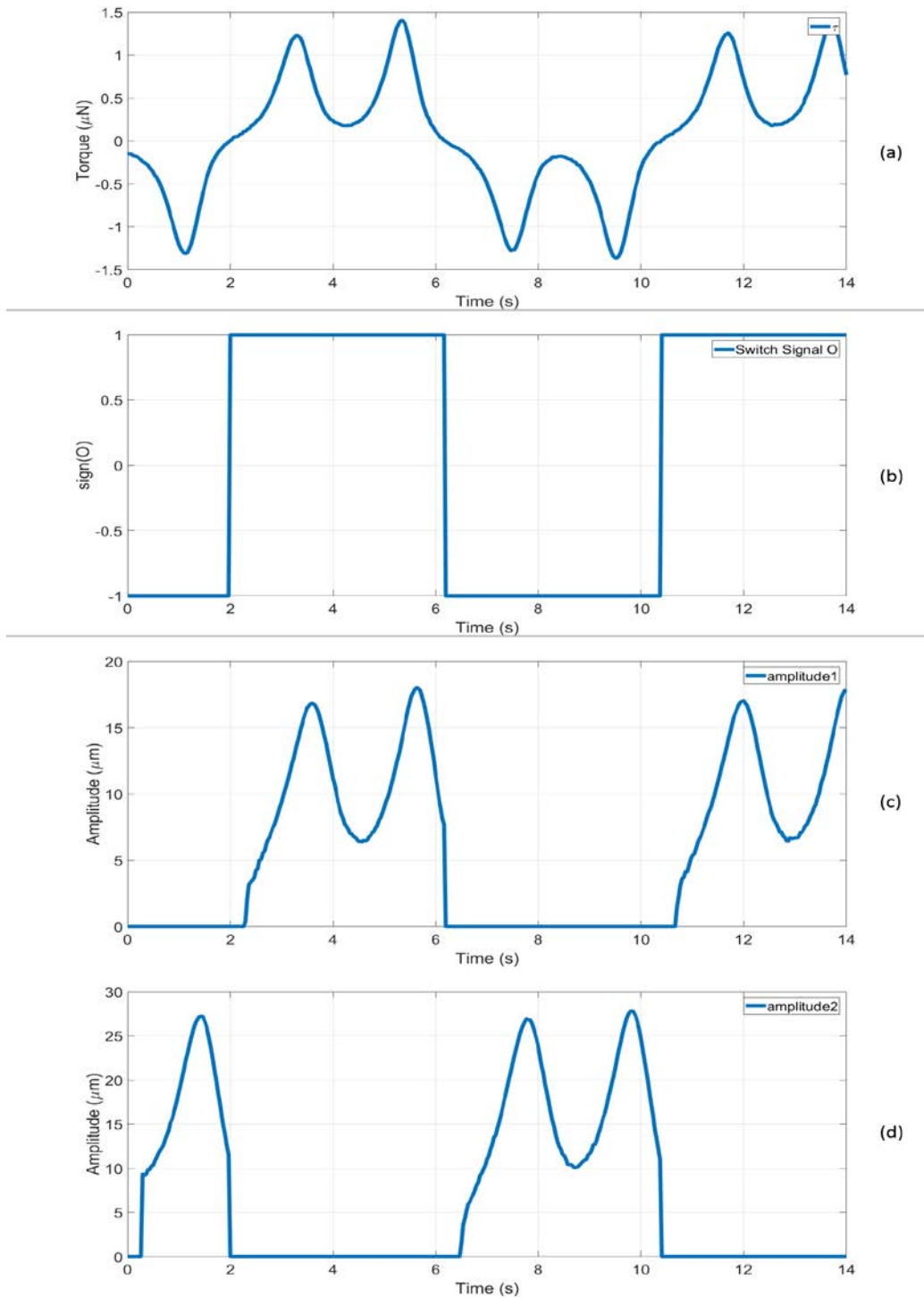This thesis presents the development of feedback motion estimator for an acoustic powered micro-swimmer. A state dependent coefficient (SDC) estimator was designed to estimate the micro-swimmer state because full state information is not available from ultrasound imaging date. An open-loop experiment was carried out to verify the features of the estimator. The performance of the estimator coupled with controller was tested in simulations. An input switch mechanism was demonstrated along with the simulation study.

The estimation procedure was firstly processed by an open-loop experiment. The micro-swimmer was activated and expected to complete a circular movement during the experiment. Both camera and ultrasound image data are collected. The former one was utilized to identify unknown parameters of the swimmer. The latter one was applied to the SDC estimator and unmeasurable states were evaluated and compared to measurements form camera. Experiment results validate that the estimator not only improves the accuracy of the measurements but also compensate the limitation of ultrasound image.

A simulation was then built to imitate a close-loop feedback control procedure. The estimator was coupled with controller to achieve a tracking task by using ultrasound image as the only feedback signal. The results indicate that the estimator works perfect with developed controller and incomplete measurement data. Based on the simulation built up, it is likely to do real-time close-loop experiment using ultrasound image feedback and SDC estimator. More,

simulation study also proves that the switch mechanism settles the restriction of unidirectional actuation issue.

Future work will firstly focus on determining a more appropriate friction model for the micro-swimmer. Next work will be on implementing real-time closed-loop experiment. Currently, real-time image data processing and transmission has been a restriction to carry out the experiment. Other restrictions come from the ultrasound imaging hardware. For instance, the memory of ultrasound machine limits a high frame rate of the image. This means the sampling frequency has to be kept low, which can create inaccuracies in the calculation of velocity from the measured position.

For micro-swimmer development, future work should be allocated on developing a micro-swimmer with a 6 degrees of freedom. More research can also be devoted to online path planning of the micro-swimmer and cooperation among multiple micro-swimmers.

APPENDIX A

STABILITY OF CONTROLLER WITH ADDITIONAL FRICTION TERMS

Substitute eq. (5.1.2) into eq. (3.2.3), the following dynamic equation can be obtained

$$M\dot{v} = \bar{\tau}_0 - D(v)v \tag{6.1.1}$$

Define auxiliary tracking error as

$$r_x = \dot{\tilde{x}} + \mu\tilde{x}, \; r_y = \dot{\tilde{y}} + \mu\tilde{y} \tag{6.1.2}$$

where μ is a scalar control gain. The auxiliary control inputs $\bar{F}_1$, $\bar{\tau}_1$ from eq. (5.1.4) and eq. (5.1.5) can be expressed as

$$\begin{bmatrix} \bar{F}_1 \\ v_3 \end{bmatrix} = T\left(u + \Pi\right) \tag{6.1.3}$$

$$\bar{\tau}_1 = \dot{u}_{d1} + \dot{v}_{3r} + k_3\eta - \omega z_2 + \tilde{z}_1 \tag{6.1.4}$$

where $T = \begin{bmatrix} r_x \sin\varphi - r_y \cos\varphi & 1 \\ 1 & 0 \end{bmatrix}$,

$$\Pi = \begin{bmatrix} v_{3r} \\ F_{1r} \cos z_1 + \dfrac{1}{m} Y_{v2} \left(\dot{y}_{rc} \cos \varphi_r - \dot{x}_{rc} \sin \varphi_r \right) \sin z_1 - \mu \left(v_1 - \dot{x}_{rc} \sin \varphi - \dot{y}_{rc} \cos \varphi \right) \end{bmatrix} \quad \text{and} \quad u = \dot{z}. \quad \text{In}$$

(6.1.4), v_{3r} and F_{1r} are reference. $z = \begin{bmatrix} z_1 & z_2 \end{bmatrix}$ is a 2×1 auxiliary tracking error vector, and it can

be expressed as

$$\begin{bmatrix} \omega \\ z_1 \\ z_2 \end{bmatrix} = \begin{bmatrix} -\tilde{\varphi} \cos \varphi + 2 \sin \varphi & -\tilde{\varphi} \sin \varphi - 2 \cos \varphi & 0 \\ 0 & 0 & 1 \\ \cos \varphi & \sin \varphi & 0 \end{bmatrix} \tag{6.1.5}$$

where ω is a scalar auxiliary error variable. In (6.1.4) u_{d1} is an auxiliary signals and can be

written as

$$\begin{bmatrix} u_{d1} & u_2 \end{bmatrix}^T = u_a - k_2 z \tag{6.1.6}$$

where u_2 is also a scalar auxiliary signals. The 2×1 auxiliary control vector u_a is defined as

$$u_a = \left(\frac{k_1 \omega + f}{\delta_d^2} \right) J z_d + \Omega_1 z_d \tag{6.1.7}$$

where k_1 is scalar gain, $z_d \in R^{2 \times 1}$ is a reference vector, $J = \begin{bmatrix} 0 & -1 \\ 1 & 0 \end{bmatrix}$. The auxiliary scalar terms

f, Ω_1 and δ_d are defined as follows

$$f = 2 \left(v_{3r} z_2 - F_{1r} \sin z_1 + \mu \left(\sin \varphi \dot{\tilde{x}} - \cos \varphi \dot{\tilde{y}} \right) \right.$$
$$\left. + \frac{2}{m} Y_{v2} \left(\left(\dot{y}_{rc} \cos \varphi_r - \dot{x}_{rc} \sin \varphi_r \right) \cos z_1 - v_2 \right) \right) \tag{6.1.8}$$

$$\Omega_1 = k_2 + \frac{\dot{\delta}_d}{\delta_d} + \frac{k_1 \omega^2 + \omega f}{\delta_d^2} \tag{6.1.9}$$

$$\delta_d = \gamma_0 \exp \left(-\gamma_1 t \right) + \varepsilon_1 \tag{6.1.10}$$

where k_2, γ_0, γ_1, ε_1 are constant scalar parameters. $\tilde{z} \in R^{2\times 1}$ is an auxiliary tracking error vector defined as

$$\tilde{z} = \begin{bmatrix} \tilde{z}_1 & \tilde{z}_2 \end{bmatrix}^T = z_d - z \qquad (6.1.11)$$

where $z_d \in R^{2\times 1}$ is a subsequently auxiliary signal. In (6.1.4), η is an auxiliary error signal which can be defined as

$$\eta = u_{d1} - u_1 \qquad (6.1.12)$$

Thus, the error dynamics of (6.1.5), (6.1.11) and (6.1.12) can be written as

$$\dot{\omega} = \begin{bmatrix} u_{d1} & u_2 \end{bmatrix} J^T z - \eta z_2 + f \qquad (6.1.13)$$

$$\dot{\tilde{z}} = \frac{\dot{\delta}_d}{\delta_d} z_d + \left(\frac{k_1 \omega + f}{\delta_d^2} + \omega \Omega_1 \right) J z_d - \begin{bmatrix} u_{d1} & u_2 \end{bmatrix}^T + \begin{bmatrix} \eta & 0 \end{bmatrix}^T \qquad (6.1.14)$$

$$\dot{\eta} = \dot{u}_{d1} + \dot{v}_{3r} - \tau_1 \qquad (6.1.15)$$

Therefore, according to *Theorem 1* proved in [34], the system of (6.1.13), (6.1.14) and (6.1.15) with tracking error (5.1.1) and (6.1.2) is GUUB.

BIBLIOGRAPHY

[1]   M. Sitti, "Voyage of the microrobots," vol. 458, no. April, pp. 1121–1122, 2009.

[2]   R. J. Dijkink, J. P. Van Der Dennen, C. D. Ohl, and A. Prosperetti, "The 'acoustic scallop': A bubble-powered actuator," *J. Micromechanics Microengineering*, vol. 16, no. 8, pp. 1653–1659, 2006.

[3]   J. Feng, J. Yuan, and S. K. Cho, "Micropropulsion by an acoustic bubble for navigating microfluidic spaces," *Lab Chip*, vol. 15, no. 6, pp. 1554–1562, 2015.

[4]   J. Feng, J. Yuan, and S. K. Cho, "2-D steering and propelling of acoustic bubble-powered microswimmers," *Lab Chip*, vol. 16, no. 12, pp. 2317–2325, 2016.

[5]   B. K. P. Horn and B. G. Schunck, "Determining optical flow," *Artif. Intell.*, vol. 17, no. 1–3, pp. 185–203, 1981.

[6]   B. D. Lucas and T. Kanade, "An iterative image registration technique with an application to stereo vision," 1981.

[7]   M. Kass, A. Witkin, and D. Terzopoulos, "Snakes: Active contour models," *Int. J. Comput. Vis.*, vol. 1, no. 4, pp. 321–331, 1988.

[8]   I. Mikic, S. Krucinski, and J. D. Thomas, "Segmentation and tracking in echocardiographic sequences: Active contours guided by optical flow estimates," *IEEE Trans. Med. Imaging*, vol. 17, no. 2, pp. 274–284, 1998.

[9]   F. Yeung, S. F. Levinson, D. Fu, and K. J. Parker, "Feature-adaptive motion tracking of ultrasound image sequences using a deformable mesh," *IEEE Trans. Med. Imaging*, vol. 17, no. 6, pp. 945–956, 1998.

[10]   M. Allen, Q. Zhong, N. Kirsch, A. Dani, W. W. Clark, and N. Sharma, "A Nonlinear Dynamics-Based Estimator for Functional Electrical Stimulation: Preliminary Results From Lower-Leg Extension Experiments," *IEEE Trans. Neural Syst. Rehabil. Eng.*, vol. 25, no. 12, pp. 2365–2374, 2017.

[11]   N. Sharma and A. Dani, "Nonlinear estimation of gait kinematics during functional electrical stimulation and orthosis-based walking," *Proc. Am. Control Conf.*, pp. 4778–4783, 2014.

[12] S. Sengupta, M. E. Ibele, and A. Sen, "Fantastic Voyage: Designing Self-Powered Nanorobots," *Angew. Chemie Int. Ed.*, vol. 51, no. 34, pp. 8434–8445, 2012.

[13] L. K. E. A. Abdelmohsen, F. Peng, Y. Tu, and D. A. Wilson, "Micro-and nano-motors for biomedical applications," *J. Mater. Chem. B*, vol. 2, no. 17, pp. 2395–2408, 2014.

[14] S. Guo, K. Sugimoto, S. Hata, J. S. J. Su, and K. Oguro, "A new type of underwater fish-like microrobot," *Proceedings. 2000 IEEE/RSJ Int. Conf. Intell. Robot. Syst. (IROS 2000) (Cat. No.00CH37113)*, vol. 2, no. 1, pp. 136–141, 2000.

[15] R. Dreyfus, J. Baudry, M. L. Roper, M. Fermigier, H. A. Stone, and J. Bibette, "Microscopic artificial swimmers," *Nature*, vol. 437, no. 7060, p. 862, 2005.

[16] A. Ghosh and P. Fischer, "Controlled propulsion of artificial magnetic nanostructured propellers," *Nano Lett.*, vol. 9, no. 6, pp. 2243–2245, 2009.

[17] L. Zhang, J. J. Abbott, L. Dong, B. E. Kratochvil, D. Bell, and B. J. Nelson, "Artificial bacterial flagella: Fabrication and magnetic control," *Appl. Phys. Lett.*, vol. 94, no. 6, 2009.

[18] C. Pawashe, S. Floyd, and M. Sitti, "Modeling and experimental characterization of an untethered magnetic micro-robot," *Int. J. Rob. Res.*, vol. 28, no. 8, pp. 1077–1094, 2009.

[19] K. B. Yesin, K. Vollmers, and B. J. Nelson, "Modeling and control of untethered biomicrorobots in a fluidic environment using electromagnetic fields," *Int. J. Rob. Res.*, vol. 25, no. 5–6, pp. 527–536, 2006.

[20] B. R. Donald, C. G. Levey, C. G. McGray, I. Paprotny, and D. Rus, "An untethered, electrostatic, globally controllable MEMS micro-robot," *J. Microelectromechanical Syst.*, vol. 15, no. 1, pp. 1–15, 2006.

[21] J. J. Abbott, K. E. Peyer, L. X. Dong, and B. J. Nelson, "How should microrobots swim?," *Springer Tracts Adv. Robot.*, vol. 66, no. STAR, pp. 157–167, 2010.

[22] A. Yilmaz, O. Javed, and M. Shah, "Object tracking," *ACM Comput. Surv.*, vol. 38, no. 4, p. 13–es, 2006.

[23] S. P. D. Purang Abolmaesumi, Septimiu E Salcudean, Wen-hong Zhu, Mohammad Reza Sirouspour, "Image-Guided Control of a Robot for Medical Ultrasound," *IEEE Trans. Robot. Autom.*, vol. 18, no. 1, pp. 11–23, 2002.

[24] S. E. Salcudean, G. Bell, S. Bachmann, W.-H. Zhu, P. Abolmaesumi, and P. D. Lawrence, "Robot-assisted diagnostic ultrasound–design and feasibility experiments," in *International Conference on Medical Image Computing and Computer-Assisted Intervention*, 1999, pp. 1062–1071.

[25] L. G. Brown, "A survey of image registration techniques," *ACM Comput. Surv.*, vol. 24, no. 4, pp. 325–376, 1992.

[26] N. Friedland and D. Adam, "Automatic ventricular cavity boundary detection from sequential ultrasound images using simulated annealing," *IEEE Trans. Med. Imaging*, vol. 8, no. 4, pp. 344–353, 1989.

[27] J. D. Pearson, "Approximation methods in optimal control I. Sub-optimal control," *Int. J. Electron.*, vol. 13, no. 5, pp. 453–469, 1962.

[28] T. Çimen, "Survey of State-Dependent Riccati Equation in Nonlinear Optimal Feedback Control Synthesis," *J. Guid. Control. Dyn.*, vol. 35, no. 4, pp. 1025–1047, 2012.

[29] R. van Hoek, M. Alirezaei, A. Schmeitz, and H. Nijmeijer, "Vehicle State Estimation Using a State Dependent Riccati Equation," *IFAC-PapersOnLine*, vol. 50, no. 1, pp. 3388–3393, 2017.

[30] D. Leith, "Drag on nonspherical objects," *Aerosol Sci. Technol.*, vol. 6, no. 2, pp. 153–161, 1987.

[31] E. Broitman, "The nature of the frictional force at the macro-, micro-, and nano-scales," *Friction*, vol. 2, no. 1, pp. 40–46, 2014.

[32] F. P. Bowden, F. P. Bowden, and D. Tabor, *The friction and lubrication of solids*, vol. 1. Oxford university press, 2001.

[33] A. D. Corwin and M. P. De Boer, "Effect of adhesion on dynamic and static friction in surface micromachining," *Appl. Phys. Lett.*, vol. 84, no. 13, pp. 2451–2453, 2004.

[34] A. Behal, D. M. Dawson, W. E. Dixon, and Y. Fang, "Tracking and regulation control of an underactuated surface vessel with nonintegrable dynamics," *IEEE Trans. Automat. Contr.*, vol. 47, no. 3, pp. 495–500, 2002.